Experimental Study on Transpiration Cooling Method through Additively Manufactured Porous Structures

Transient Experiments Using Thermochromic Liquid Crystals

Sylwia Kozlowska

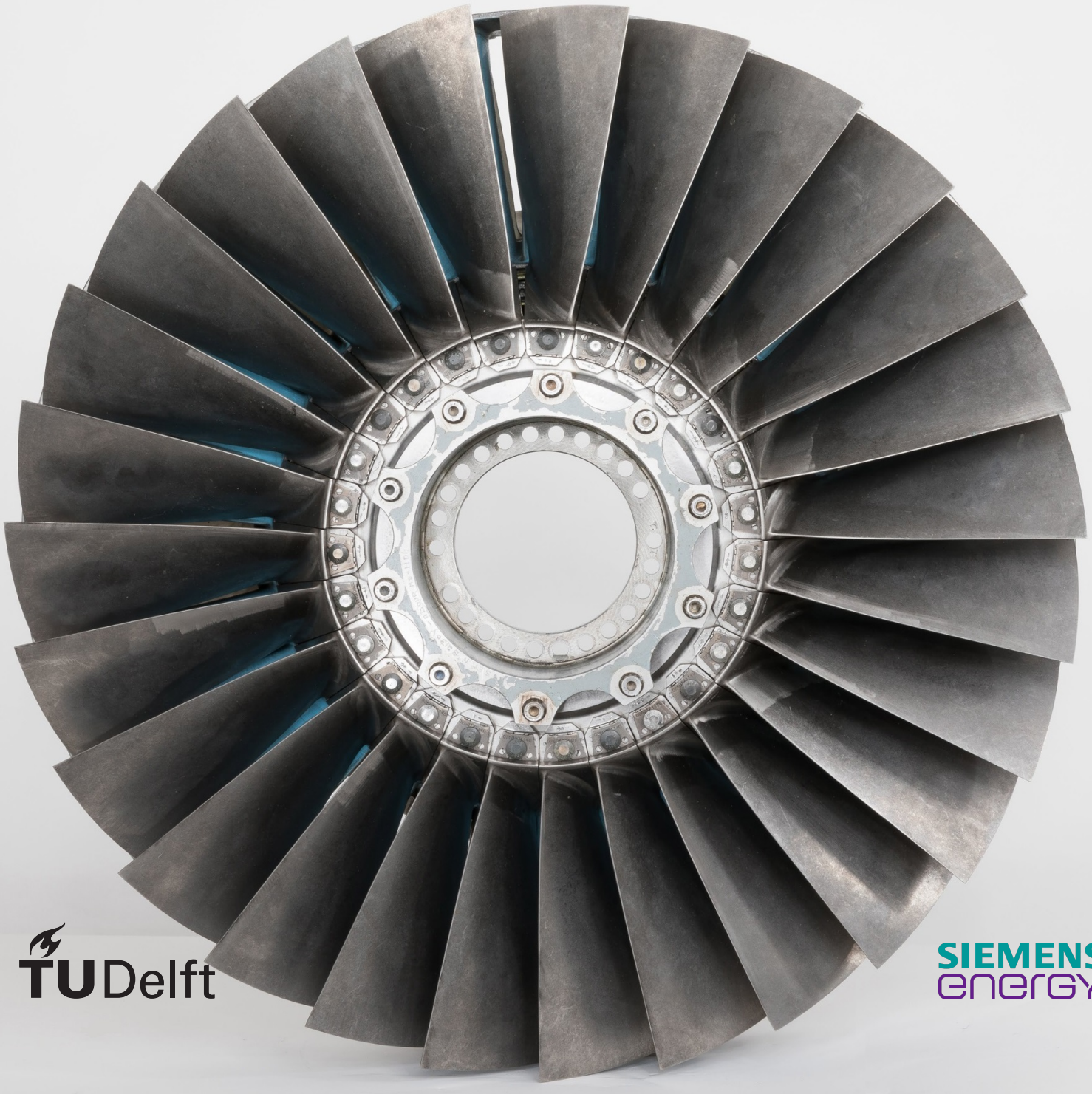

Technische Universiteit Delft

TU Delft

SIEMENS energy

Experimental Study on Transpiration Cooling Method through Additively Manufactured Porous Structures

Transient Experiments Using Thermochromic Liquid Crystals

by

Sylwia Kozlowska

to obtain the degree of Master of Science
at the Delft University of Technology,
to be defended publicly on Tuesday August 24, 2021 at 10:00 AM.

Student number:	4458575	
Project duration:	September 1, 2020 – August 24, 2021	
Thesis committee:	Prof. Ir. Clemens A. Dransfeld	TU Delft, chair holder
	Asst. Prof. Ir. Jos Sinke,	TU Delft, supervisor
	Asst. Prof. Dr. Ir. John-Alan Pascoe	TU Delft, examiner
	Dr. Ir. Mats Kinell,	Siemens Energy, supervisor

An electronic version of this thesis is available at `http://repository.tudelft.nl/`.

TU Delft

Preface

On a professional note, first and foremost, I would like to express my gratitude to my industrial supervisor Dr. Ir. M. Kinell for giving me the opportunity to do my thesis at Siemens Energy and for helping me with all the technical aspects of the research. Furthermore, I want to extend my gratitude to my university supervisor, Asst. Prof. Ir. J. Sinke. Thank you for agreeing to be my supervisor and for the continuous support and guidance throughout my thesis.

On a personal note, I must thank my parents and siblings. Without them, I would not be where I am today. They encouraged me to reach for my dreams, supported me through my education and gave me strength when I needed it the most. Especially my wonderful sister, Inga, who was willingly listening to all the hardships I have encountered and inspired me to keep going. Further thanks, to my partner, Mintu, who has motivated me and lifted my spirits whenever I was feeling down.

Special thanks to Anna, my partner in crime in the Fluid Dynamics Lab. Our countless lunches and Fika breaks will stay with me forever. I would also like to thank all my friends and coworkers from Siemens Energy that made my time in Sweden, during a crazy pandemic time, an amazing adventure, one that I will never forget.

Of course, many thanks to my friends from the Delft University of Technology. Your support and kindness motivated me throughout my time in the Netherlands. Special thanks to my friend Nathan, who always had my back and never gave up on me.

I would also like to thank friends, colleagues, professors and other academic staff I have met throughout my years at Delft University, you truly made my education a wonderful experience.

Sylwia Kozlowska
Kielce, August 2021

Contents

Page number

Nomenclature

$\dot{m}$	Mass flow ($\frac{g}{s}$)
A	Area (m^2)
C_p	Specific heat capacity ($\frac{J}{K}$)
D	Diameter of a film cooling hole (mm)
H	Height (mm)
h	Heat transfer coefficient ($\frac{W}{m^2K}$)
K	Sensitivity matrix (-)
L	Stream-wise dimension of the porous structure (mm)
M	Blowing ratio (-)
P	Pressure ratio (-)
q	Heat Flux ($\frac{W}{m^2}$)
Re	Reynolds number (-)
T	Temperature (^oC)
U	Uncertainty (-)
v	Velocity ($\frac{m}{s}$)
W	Width (mm)
x	Downstream length (mm)

Greek symbols

δ	Thickness of the test plate (mm)
η	Film Cooling Effectiveness(-)
ϕ	Overall cooling effectiveness (-)
ρ	Density ($\frac{kg}{m^3}$)
σ	Standard deviation (-)
λ	Heat conductivity ($\frac{W}{mK}$)

Subscripts

C	Related to coolant flow
g	Related to maximum green intensity
h	Hydrualic
i	Related to initial conditions

M	Related to mainstream flow
o	Related to a non-cooled test
p	Parameters
R	Related to the reference flow
r	Related to maximum red intensity
W	Related to adiabatic wall

Abbreviation

AM	Additive Manufacturing (-)
HSV	Hue, Saturation, Value colourspace (-)
RGB	Red, Green, Blue colourspace (-)
ROI	Region of Interest
SC	Single crystals (-)
SMC	Special Metals Corporation
TLC	Thermochromic Liquid Crystals (-)
$TTLC$	Thermotropic Liquid Crystals (-)

List of Tables

List of Figures

1 Introduction

Gas turbines are important part of our daily life. Due to their compact size they often serve as a back-up power generators either in hospitals or remote areas. However, they are not environmentally-friendly. With the global effort to reduce the emissions, there is a need to improve gas turbines' efficiency. This chapter is structured in the following way, in Section 1.1 contains the project motivation together with an a literature review about current state of external cooling methods for turbine blades. Section 1.2 lists the research questions that will be answered in this report. Finally, section 1.3 provides the thesis outline for this report.

1.1. Project motivation

The motivation for this project emerged from the constant need to improve turbine efficiencies. A turbine is a last stage of the gas turbine, responsible for harvesting kinetic energy and turning it into into a rotational motion. It consists of rows of airfoil cascades mounted on a shaft. These airfoils are subjected to very high temperatures. The temperatures the blades and vanes can safely withstand are proportional to the thermal efficiency of the turbine. The blades need to be protected from incoming hot air by many sophisticated cooling techniques and protective coatings. This thesis will only focus on the cooling techniques. One well-known methods, film cooling, comes with several disadvantages. The biggest disadvantages are non-uniform cooling performance due to discretized hole locations where the areas between holes are not cooled and limited operational conditions; film cooling is the most effective for a slim range of operating conditions.

In film cooling air is pushed through rows of holes to the external surface of the blade. The air that is used for film cooling is compressed air that enters the gas turbine. Currently, about 20% of the compressor air is circumvented around the combustion chamber and fed directly to turbine components such as vanes or blades [1]. There it flows through the internal system of channels exchanging heat with e.g. the airfoil of a blade, to be finally expelled through the trailing edge of the blade or the rows of film cooling holes located across the blade. Once the air is ejected through the film cooling holes, it forms a protective layer of cooler air on the (external) surface of the blade. Preventing the hot air coming from a combustion chamber from damaging the blade's surface.

Originally, the idea of having air expelled outside the blade is from the 1960s [2], however, the the design used today was introduced in the 1990s [3]. Since the performance of the film cooling is influenced by its design parameters such as hole diameter and shape, hole spacing, number of holes, injection angle and relative momentum of the coolant air to the hot mainstream air, multiple studies have been conducted over the years to find the most optimal design. Baheri et al. [4] investigated how different shapes of film cooling holes influence cooling performance. Out of the four shapes studied (1) cylindrical film hole; (2) 15^o forward diffused film hole; (3) trenched cylindrical film hole; (4) trenched 15^o forward-diffused film hole, the last one showed the highest film cooling effectiveness, both spanwise and streamwise. Whereas Wang et al. [5] studied (1) cylindrical hole; (2) combined hole (3-in-1); (3) conical hole; (4) fan-shaped hole. The combined hole provided the most uniform protection and had better cooling performance than other configurations. Additionally, simple cylindrical hole configuration proved to have the lowest lateral-averaged film cooling effectiveness. In both studies, the most optimal design was found to have a complex shape as compared to simple cylindrical hole.

Many of the sophisticated film cooling designs, are expensive and difficult to manufacture in metal, using traditional metal manufacturing techniques like milling or lathing. Only with the development in the Additive Manufacturing (AM) did it become possible to manufacture some more complex deigns in nickel alloys, material used to manufacture gas turbine's vanes and blades. Snyder and Thole [6] manufactured six different film cooling coupons: 777 [7], console [8], crescent [9], oscillator [10][11], spiral [11] and tripod film cooling holes [12]. All coupons were manufactured using the laser powder bed fusion method. The study proved that Additive Manufacturing is capable to manufacture complex cooling shapes in metals but also demonstrated the differences in the cooling performance as compared to the same designs manufactured in polymers. In the future, this manufacturing method might allow more complicated film cooling shapes to be implemented on an industrial scale.

As mentioned earlier, the biggest drawback of cylindrical film cooling shape is its non-uniform cooling of the sample. To address this issue, the idea of transpiration cooling was proposed. Transpiration cooling is a special case of film cooling, where the coolant air is pushed through, or sweat through, a uniform porous structure, rather than rows of holes. Recent developments in Additive Manufacturing allowed to manufacture such structures using Laser Powder Bed Fusion (LPBF).

First studies conducted on transpiration cooling focused on the temperature of the porous structure itself. Studies conducted by Ding [13] and Huang [14] investigated the cooling of a sintered porous flat plate. Huang tested porous plates made from bronze and stainless steel. He found that increasing the thermal conductivity reduced the temperature and temperature nonuniformities of the porous surface. Whereas Ding found that for the same blowing ratio, the cooling effectiveness increases with the increasing mainstream Reynolds number. Other researchers, Huang et al. [15] investigated the mechanical and cooling properties of flat plates made of blended, alternating regions of porous (perforated) areas and solid partition walls. The ultimate tensile strength (UTS) increased by 440% for the porous plate with partition walls as compared to a sintered porous plate. At the blowing ratio of M=0.02, the plates with partition walls had nearly the same cooling effectiveness as a sintered porous plate. However, for blowing ratio M=0.03, the sintered porous plate had better cooling effectiveness than any other sample. For real-life application the performance in the downstream region of a porous structure also needs to be known.

The first research into the downstream cooling performance of a transpiration cooling plate was by Fier and Bogard **[18]**. They investigated the downstream cooling performance of a 3D printed, plastic lattice structure with a 30% through-flow area. The results showed that for increasing velocity ratio, defined as the ratio of coolant velocity to the mainstream velocity, laterally averaged adiabatic cooling effectiveness increases. However, for all the velocity ratios, the cooling effectiveness rapidly decreases in the upstream flow direction, especially in the region right after the sample. Plastic is not a suitable material to be used on the turbines blades, therefore, there is still a knowledge gap when it comes to a downstream performance of the metallic transpiration cooling structures.

This study will address this issue. It will investigate the downstream cooling performance of additively manufactured metallic porous transpiration cooling structures using Thermochromic Liquid Crystals (TLC) using a heat transfer rig. The performance will be measured by calculating the heat transfer coefficient and film cooling effectiveness downstream of the porous sample. In addition, the distribution uniformity of the pores will be studied in a water visualization rig.

1.2. Research questions

This research will try to answer questions from two main categories. First category relates to transpiration cooling and what influences the performance. Therefore, the first research question formed:

> 1: What is the downstream performance of a additively manufactured metallic porous transpiration cooling structure?

This can be directly split into four more specific sub-questions that relate the performance to specific testing properties or properties of the samples :

1A: How do different blowing ratios influence downstream performance?

1B: How does the thickness of porous structure influence the downstream performance?

1C: How does through-flow area influence the downstream performance?

1D: How does the type of the material influence the downstream performance?

The other category is comparison of transpiration cooling to the film cooling Therefore, the second main question is formed as:

2: How does transpiration cooling performance compare to film cooling performance?

1.3. Thesis outline

The thesis is structured as follows. In Chapter 2 theoretical background information about gas turbines, cooling methods, thermodynamic liquid crystals and additive manufacturing is present. In Chapter 3 the theory behind the experiment is explained. In Chapter 4 the set-up, experiment and rig validation is shown. The results obtained from the experiment are shown in Chapter 5 followed by the discussion in Chapter 6. In Chapter 7 the conclusions based on the obtained observations are given together with the recommendations for future work.

2

Background information

This chapter provides a background information, necessary to understand the methodology of this experiment. The chapter begins with a Section 2.1 that provides the information about gas turbines, their working principle and the challenges encountered. This is followed by a Section 2.2 about Thermochromic Liquid Crystals (TLC) explaining where TLCs fit within the Liquid Crystals family and the physics behind them. Subsequently, Red Green Blue (RGB) colour system and Hue Saturation Value (HSV) colour system will be explained and compared in Section 2.3. In the last Section 2.4 the study of Additive Manufacturing is presented, together with explanation on additively manufactured porous media.

2.1. Industrial gas turbines

A gas turbine, commonly referred to as a combustion turbine, is a type of continuous, internal combustion engine. The main three elements of turbines are: a rotating gas compressor, a combustion section and a turbine on the same shaft as the compressor. For each of these components multiple designs are in use. The three main types of gas compressors are: axial compressor, centrifugal compressor and a mixed flow compressor. The next stage is a combustion chamber. It is typically made out of rings of fuel injectors, which inject fuel into the chamber where the fuel is mixed and burnt. The last stage, a turbine, consists of rows of airfoil cascades. There are 2 different types of rows. The first type, called the rotor, is connected to the central shaft and rotates at high speed. The second type, called the stator, is fixed and does not rotate [16]. The gas turbine layout can be seen in Figure 2.1.

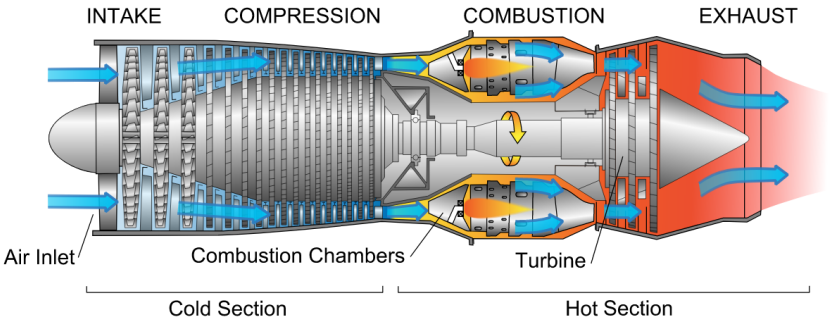

Figure 2.1: *Schematics of a gas turbine [17]*

Process

Each stage of a gas turbine have specific functions. The compressor serves three functions, it draws air inside, compresses the air and pushes the air to the combustion chamber. In the combustion chamber, the air is mixed with the injected fuel, then this mixture is ignited and burnt. The process of combustion produces high temperature and high-pressure gas that enters next stage, the turbine. The gas expands in the turbine spinning the rotating blades to generate power and exits the gas turbine. In some turbines, an additional heat recovery steam generator is mounted on the turbine exhausts to increase the efficiency.

The gas turbine undergoes a process similar to a Brayton cycle. During the Brayton cycle, the gas undergoes four thermodynamic processes. Isentropic compression in the inlet and in the compressor(process a-b), constant pressure fuel combustion(process b-c), isentropic expansion in the turbine (process c-d) and heat rejection(cooling the air at constant pressure, process d-a), this process can seen in Figure 2.2. The ideal Brayton cycle assumes that the compressor and the turbine undergo isentropic processes, when the entropy of the system is not changing. However, in real gas turbines there are losses attributed to irreversible energy transformation such as internal friction and turbulence, therefore, making these processes not isentropic.

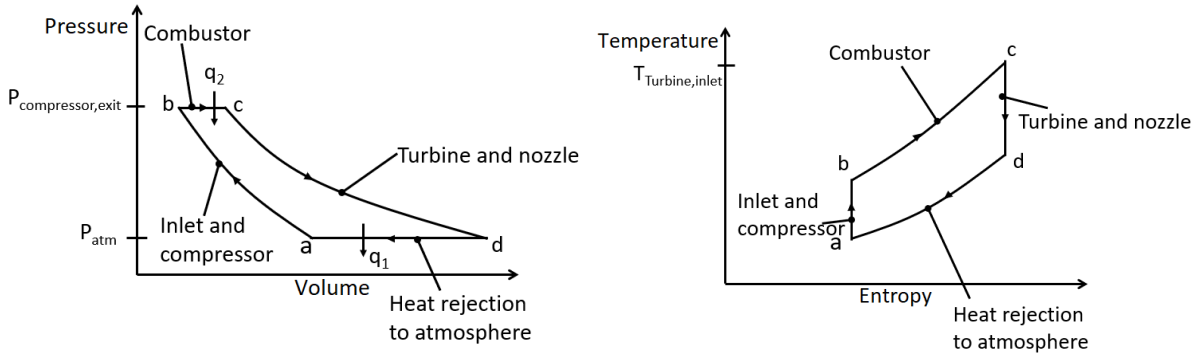

(a) *Ideal Brayton cycle pressure vs. volume diagram*

(b) *Ideal Brayton cycle temperature vs. entropy diagram*

Figure 2.2: *Ideal Brayton cycle*

Efficiency

Efficiency is the critical aspect of a gas turbine. The temperature at which the turbine operates is proportional to its efficiency. The thermal efficiency is calculated in a following way:

$$\eta_{brayton} = \frac{Q_{in} - Q_{out}}{Q_{in}} \tag{2.1}$$

where Q is the energy. The energy added, Q_{in} is equal to $Q_{in} = mC_p(T_c - T_b)$ whereas energy rejected is equal to $Q_{out} = mC_p(T_d - T_a)$. When substituted in Equation 2.1 gives:

$$\eta_{brayton} = 1 - \frac{T_d - T_a}{T_c - T_b} = 1 - \frac{T_d\left(1 - \frac{T_a}{T_d}\right)}{T_c\left(1 - \frac{T_b}{T_c}\right)} \tag{2.2}$$

The pressure ratio of the Brayton cycle, r_p is defined as:

$$r_p = \frac{P_b}{P_a} \tag{2.3}$$

Therefore:

$$\frac{P_b}{P_a} = \frac{P_c}{P_d} \tag{2.4}$$

The processes a-b and c-d are isentropic. Hence,

$$\frac{T_b}{T_a} = \left(\frac{P_b}{P_a}\right)^{\frac{\gamma-1}{\gamma}} \tag{2.5}$$

and similarly:

$$\frac{T_c}{T_d} = \left(\frac{P_c}{P_d}\right)^{\frac{\gamma-1}{\gamma}} \tag{2.6}$$

combining equations 2.4, 2.5 and 2.6 gives ratio of temperatures:

$$\frac{T_b}{T_a} = \frac{T_c}{T_d} \tag{2.7}$$

combining equations 2.7 and 2.2 gives:

$$\eta_{brayton} = 1 - \frac{T_d}{T_c} \tag{2.8}$$

This shows that the efficiency of the Brayton cycle is dependent on the turbine's inlet temperature.
To push the limits of the turbine's inlet temperature, over the years manufacturers have developed more and more sophisticated solutions to protect turbine's metal components from thermal damage. First turbine blades were solid parts, withstanding the temperature of about 980^oC, which was limited by the metal melting point. Later convection blades were invented, with internal channels passing through them, to eventually further evolve into film convection, which allowed to raise the temperature to approximately 1530^oC. If transpiration cooling is proven successfully, this temperature can be further increased to about 1930^oC [3].

2.1.1. Cooling methods

There are many methods of turbine blade cooling. The two main categories are internal and external cooling methods. The external cooling techniques include, amongst others, film cooling, cooling effusion, pin fin and transpiration cooling. The internal cooling techniques include convection and impingement cooling. Their respective processes are described below. Some of the cooling methods are visualised in Figure 2.3.

Convection cooling
Convection cooling is the oldest cooling method. In this method, the cool air from the compressor flows inside the nozzles and rotor blades [18]. This process removes the heat from the blade material by simple convection process. Typically, the air re-enters the outside of the vanes at the blade tip and the trailing edge.

Impingement cooling
Impingement cooling is a special case of convection cooling. It works by hitting the inner surface of the blade with high velocity cool air that comes from the compressor stage of the gas turbine. This process allows more heat to be transferred by convection than in a regular convection cooling process. Typically it is used in the areas with the highest temperature, in case of a the turbine blade, it would be at the leading edge.

Film cooling
Another technique, film cooling, is a widely used technique in turbine blade cooling. In this technique coolant air is pumped out of the blade through multiple small round holes in the structure, creating a thin layer (often referred to as a film) of cool air on the external surface of the blade, this reduces the heat transfer from the incoming hot flow to the blade. One of the biggest disadvantage is its uniformity: areas between the holes are not cooled effectively.

Pin fin cooling
Pin fin cooling it typically used in the trailing edge of the turbine blade. In this technique there is an array of pin fins on the blade's internal surface. In this process coolant flows across the area with the pin fins with a high velocity, the flow separates when it hits the fins creating wakes. The cooling rate depends on many factors such as type of pin fins, its size and geometry and spacing between them.

Transpiration cooling
Similarly to film cooling, transpiration cooling also creates a thin film of cooling air on the blade. However, in the case of transpiration cooling, the air is 'leaked' through the porous material. Transpiration cooling is more effective because it uniformly covers the entire surface of the blade with cool air.

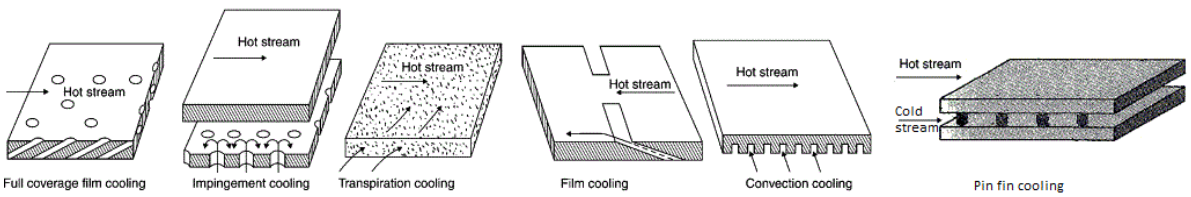

Figure 2.3: *Cooling types [19]*

In gas turbines, there are many cooling methods applied. Typically, it is a combination of film cooling, impingement cooling and pin fin cooling. However, different manufacturers will use different combinations of these methods.

2.1.2. Cooling parameters

Cooling techniques are characterised by many parameters, these parameters need to be optimised in order to get the best cooling performance. The most important ones are film cooling effectiveness and heat transfer coefficient.

Film cooling Effectiveness

The two main parameters that define a cooling process are the film cooling effectiveness and the heat transfer coefficient. Film cooling effectiveness is a function of the temperature of the main flow (T_M), the temperature of the coolant flow (T_C) and adiabatic wall temperature (T_w):

$$\eta = \frac{T_M - T_w}{T_M - T_C} \tag{2.9}$$

The film cooling effectiveness is in the range 0-1. For perfect cooling performance, the film cooling effectiveness would have a value of $\eta = 1.0$, this would be the case when T_w would be equal to the coolant temperature; while a value of $\eta = 0$ would indicate that the cooling has no effect on the temperature of the wall. As such, the goal for all cooling techniques is to maximise the cooling effectiveness. In practice, for the film cooling, the effectiveness is the highest immediately downstream to the holes and decreases rapidly in the streamwise direction, due to turbulent dispersion of the coolant [20]. This is illustrated in Figure 2.4.

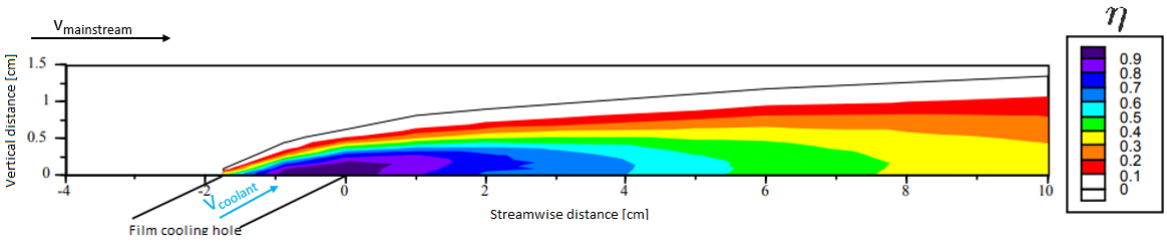

Figure 2.4: *Thermal profiles showing the coolant distribution flowing from a film cooling hole adapted from [20]*

Heat transfer coefficient

The heat transfer coefficient is a constant that characterises the convective heat transfer between a fluid medium (a fluid) and the surface (wall) flowed over by the fluid. The unit definition of the heat transfer coefficient is heat per unit area per kelvin$\left(\frac{W}{m^2K}\right)$. It is defined as the heat flux (q) divided by the temperature difference:

$$h = \frac{q}{\Delta T} \tag{2.10}$$

The cooling techniques aim to reduce convective heat transfer to the surface. Therefore, the goal is to minimise the heat transfer coefficient.

2.1.3. Materials

As stated before, the limiting factor in the material selection for the turbine blades was the thermal properties of the materials. In the early stages of gas turbine development the Nimonic, produced by Special Metals Corporation (SMC), was used. The Nimonic refers to a family of Nickel super-alloys. These alloys consist of nickel (more than 50%), chromium (around 20%) and additives such as cobalt, aluminium or titanium. Other inventions in material science that allowed for higher temperatures were directional solidification (DS) and single crystal (SC) manufacturing methods. These methods were based on a notion that grain boundaries weaken the structure because on the grain boundary creep, corrosion, oxidation and micro-cracks can occur. In DS process, the crystals form parallel to each other. It is achieved by slowly drawing out a form from a furnace into a coolant. The crystals begin to form on the cold side of the form and progressively elongate across the temperature gradient. The columnar grains are aligned with the stress axis (root to tip direction) of the blade resulting in a significant improvement in creep and thermal fatigue properties. In SC manufacturing, the technology goes one step further, creating a structure with no grain boundaries, to further increase the performance. In the 1970s, a team of researches found out that by solidifying a molten super-alloy directionally, starting at the root of a bent structure (see Figure 2.5), also known as the grain selector, it naturally

filtered the crystals and allowed only one crystal into the mould, where the buildup of a single crystal blade started. The schematics of this casting process are shown in Figure 2.6.

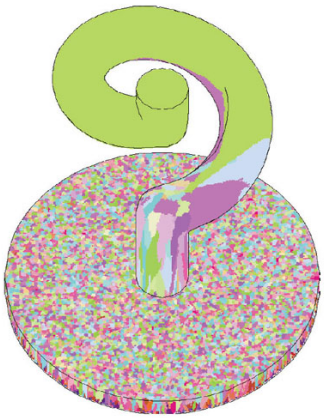

Figure 2.5: *Single Crystal smooth bent structure [21]*

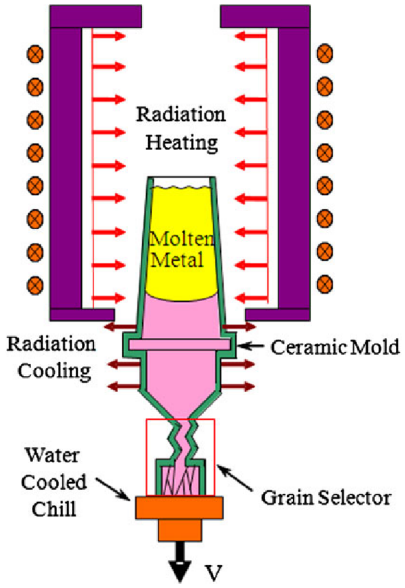

Figure 2.6: *Casting schematics [22]*

2.2. Thermochromic Liquid Crystals

Liquid crystals (LCs) are a state of matter which has properties between conventional liquids and solid crystals. Liquid crystals are divided into two main categories: Lyoropic and Thermotropic. The Thermotropic Liquid Crystals the Liquid crystal phase is dependent on the temperature [23], whereas in Lyotropic Liquid Crystals this phase is dependent on the concentration of the material. Lyotropic Liquid Crystals typically are made of mixtures of amphiphilic (hydrophobic on one end and hydrophilic on the other) molecules and a solvent. An example in daily life of a Lyoropic liquid crystals is a mixture of soap and water.

Thermotropic Liquid Crystals can be further divided into Smectic and Nematic Liquid crystals. In both, the molecule axes are parallel to each other. The difference is how the molecular centre of gravity moves. In Smectic liquid crystals, it moves in 2-dimensional planes and in Nematic Liquid crystals it moves in 3-dimensions. Further classification of Nematic Liquid crystals is Non-optically active (Nematic) and Optically-Active (Cholesteric). The division can be seen in Figure 2.7.
Thermochromic Liquid Crystals are a special type of liquid crystals, because they change colour with temperature. TLC belong to Optically-Active category of Nematic Liquid Crystals. They can have different formulations comprising of cholesterol and other sterol derived chemicals (cholesteric TLCs), formulations comprised entirely of non-sterol based chemicals (Chiral Nematics) or combination of sterol and non-sterol chemicals [23].

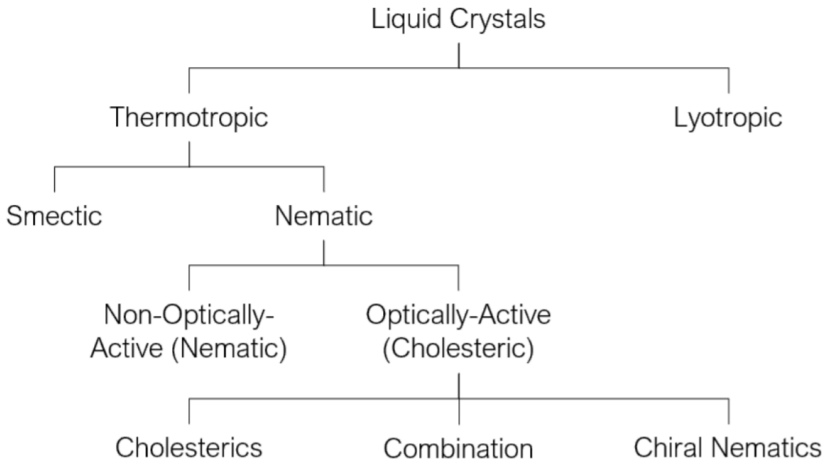

Figure 2.7: *Classification of Liquid Crystals [23]*

Figure 2.8 shows the phase changes of TLC with increasing/decreasing temperature. In the beginning, the solid crystal molecules are well-organised, with each molecule having the same orientation in layers. When the temperature increases cholesteric liquid crystals start to twist in different directions, with the increasing twisting angle. When the first layer twists clockwise by ψ degrees, the next layer will also twist clockwise by ψ degrees with respect to the previous layer. This continues for each consecutive layer.

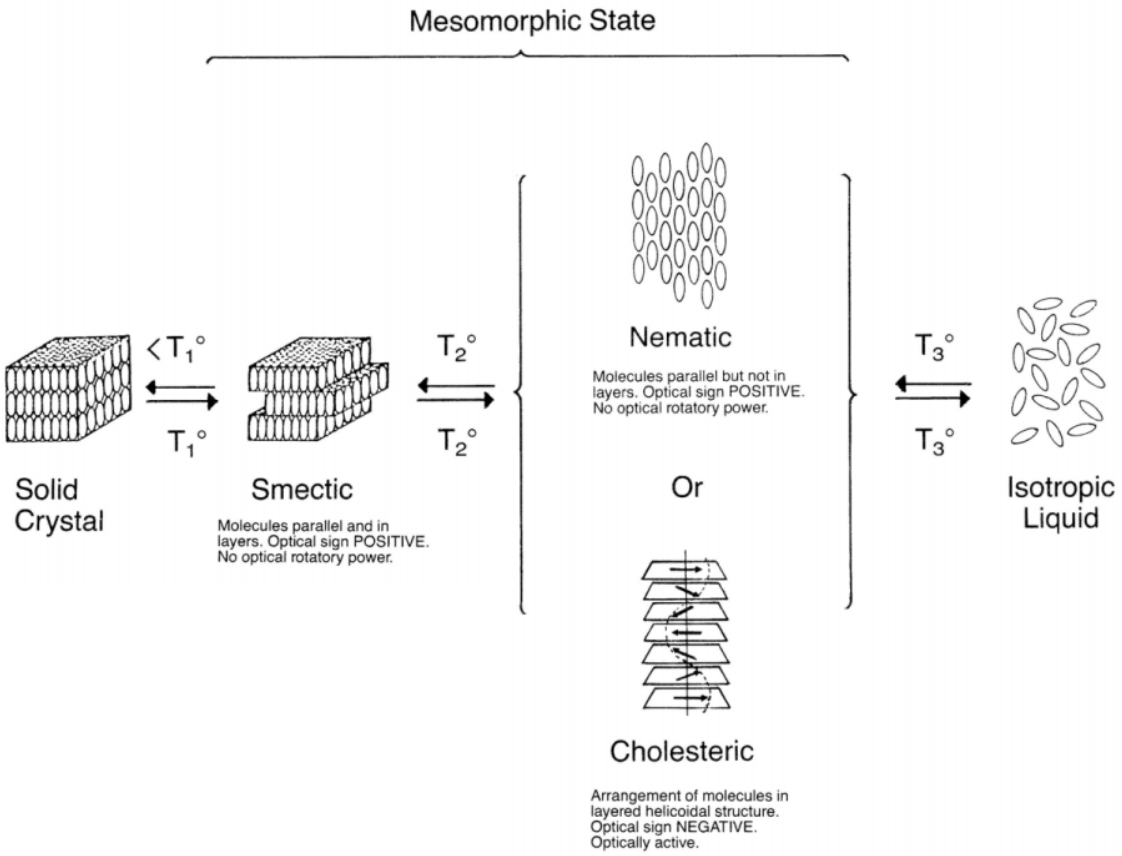

Figure 2.8: *Thermochromic Liquid Crystals phase changes with temperature [23]*

TLC can be divided into two groups: temperature-sensitive and temperature-insensitive, based on how many colours they can display. The temperature-sensitive starts in a transparent condition, then shift to red, green,

blue and back to transparent. These colour shifts are marked by four key points named: the Red Start, Green Start, Blue Start and Clearing Point respectively. Another key feature is the bandwidth, which is defined as the temperature range between Red Start point and Blue Start point, see Figure 2.9. The temperature-insensitive TLC, also known as shear-sensitive show only two colours. One below and one above the clearing point as can be seen in Figure 2.10

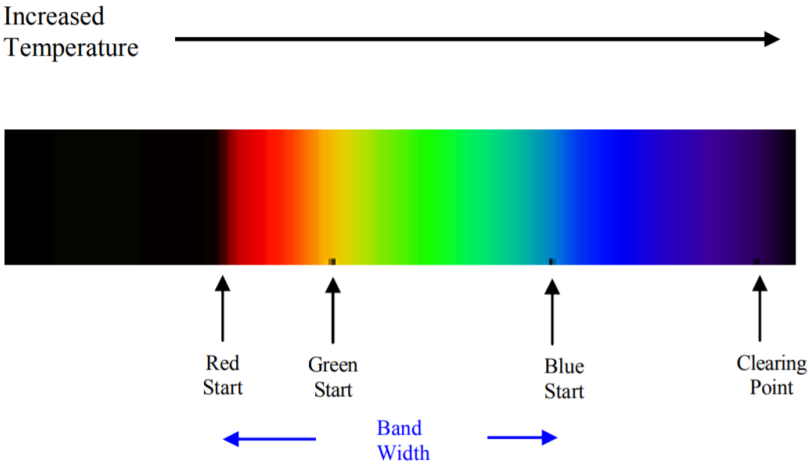

Figure 2.9: *Colour spectrum of temperature-sensitive TLC [23]*

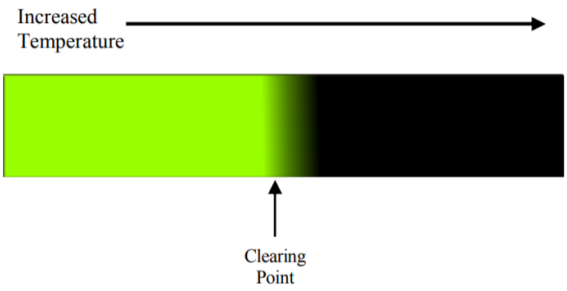

Figure 2.10: *Colour spectrum of temperature-insensitive TLC [23]*

The mechanism of thermochromism has many applications. For high-precision applications such as colour mapping of the flows, thermometers, refrigerators or medical use TLCs are used. TCLs have some limitations. One such limitation is that to manufacture TLCs expensive, specialised equipment is required. Their lifespan is limited and depends on the conditions they are subjected to such as ultraviolet radiation (UV) or high temperatures. TLCs are also very sensitive to organic chemicals, especially fats, greases and common solvents [23]. The shear sensitive Leuco dye that changes colour with light or heat, is typically used for the low-precision applications such as thermochromic t-shirts, mugs or battery state indicator[1].

2.3. Colour spaces

Colour spaces are organised and defined collections of colours. For the purpose of this experiment the Hue, Saturation, Value (HSV) and the Red, Green, Blue (RGB) colour spaces have been considered. The RGB is an additive colour space, which means that any final colour can be achieved by combination of 3 primary colours; red, green and blue. The colour space can be visualised as a unit cube with red, green and blue as x-,y-, and z-axis of the cube, see Figure 2.11. As opposed to RGB, HSV colour space can be visualised as a cylinder in polar coordinate system, with the z-axis being value, radial coordinate being saturation and angular coordinate being hue which is depicted in Figure 2.12.

[1] Leuco dye is not a TLC, but it has thermochromic properties

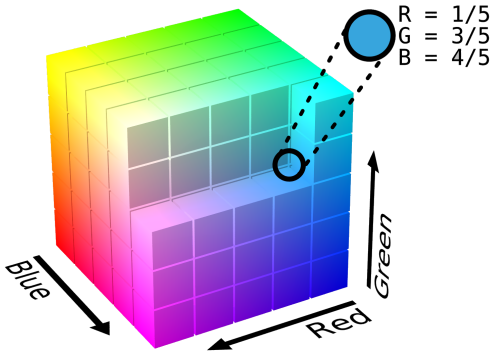

Figure 2.11: *RGB unit cube [24]*

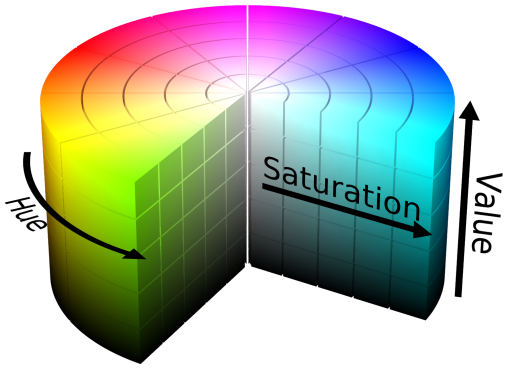

Figure 2.12: *HSV cylinder [25]*

To achieve stable measurement from the TLC sheet, the colour spaces need to have distinctive features. In case of TLC, the intensity of colours will be changing with time. The RGB and HSV calibration output curves for the TLC sheet used in this experiment are presented in Figure 2.13a and 2.13b respectively.

The RGB colour space has three characteristic curves for: red, green and blue. The peaks for red and green colour are clearly defined. Whereas the blue colour peak is not as prominent. When a crystal reaches a green peak it means that it has reached the most intense green colour. This characteristic is important because it is possible to experimentally determine the temperature at which that point is achieved. The HSV output curves also consist of three curves: Hue, Saturation and Value. The curves seem to be more scattered when comparing to RGB output curves. At about $T = 35.7^{o}C$ the TLCs went back to the initial black colour, hence the sudden drop in both colour spaces. As explained by Ke [26] and Billot [27], the HSV colour space was proven to give numerically unstable solutions. Therefore, for the rest of this experiment RGB colour space is used.

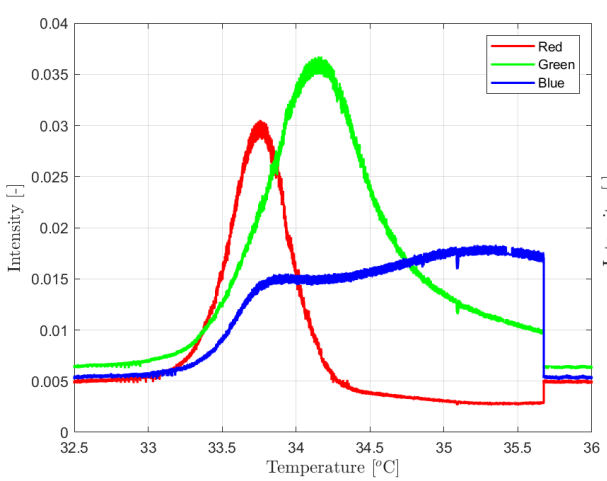

(a) *RGB calibration output curves*

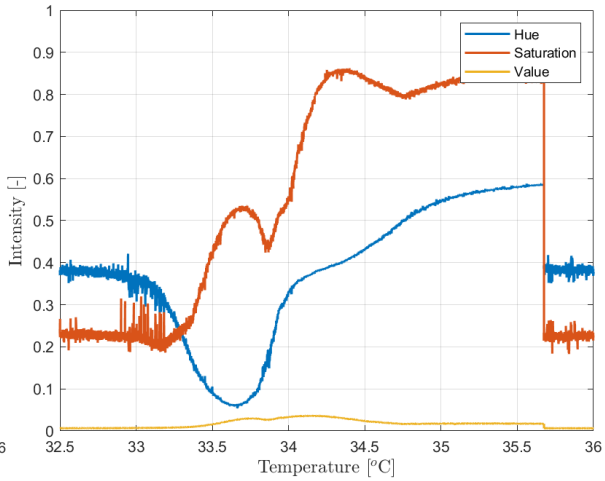

(b) *HSV calibration output curves*

Figure 2.13: *Different colours spaces for calibration outputs*

2.4. Additive Manufacturing

Additive Manufacturing can be divided into seven different process types: Binder Jetting, Direct Energy Deposition, Material Extrusion, Material Jetting, Powder Bed Fusion, Sheet Lamination and Vat Polymerisation. Table 2.1 briefly summarise them all. For this experiment, samples were manufactured using Powder Bed Fusion. Therefore, the details of this process will be further explained.

Table 2.1: *Additive Manufacturing processes*

Type	Description
Binder Jetting	Liquid bonding agent is deposited to join powder
Direct Energy Deposition	Thermal energy melts materials when deposited
Material Extrusion	Materials are selectively dispensed from the nozzle(s) or orifice
Material Jetting	Droplets of build material are selectively deposited
Powder Bed Fusion	Thermal Energy selectively fuses powder bed regions
Sheet Lamination	Material sheets are bonded
VAT Polymerisation	Liquid photo-polymer selectively cured by light-activated polymerisation

Powder Bed Fusion utilises fine metallic powder and laser or an electron beam to fuse the powder. The process takes place in a heated vacuum chamber. On the build plate a thin layer of powder is deposited using a roller. Next, the laser or electron beam fuses the powder in the 2D plane. The build plate then lowers and the process is repeated until the whole part is completed. The unfused powder that resides within the build space is removed and can be used for other builds. Once the process is finished, the build plate is removed from the machine and placed in the bead blasting machine to get rid of any residue powder. When there is no remaining powder, the parts need to be removed from the build plate.

Powder Bed Fusion is an ideal process for manufacturing complex prototypes that could not be produced by conventional methods such as Computerized Numerical Control (CNC) milling or turning. As opposed to the subtractive manufacturing, in Powder Bed Fusion process most of the powder can be reused without any post-processing such as melting or atomisation.

However, Powder Bed Fusion process has also many disadvantages such as the initial cost of the machine, software required, raw materials and labour cost. The operator of the machine needs to be highly trained in order to obtain defect-free parts. The price of the machine varies from 100 000 US dollars to 650 000 US dollars [28], depending on the manufacturer and machine capabilities. The size of the part manufactured is also limited by the build plate. The typical dimensions are approximately 200x200x350mm (based on Arcam A2) [29]. The production time of the Powder Bed Fusion process is long and depends on the complexity of a part to be built. Due to the nature of the process, it is difficult to increase production rates, without decreasing the quality of the part. As Powder Bed Fusion is a new technology, the full potential of the technology is yet to be reached.

Additively Manufactured Porous Media

Porous materials are characterised by their sponge-like structure. The structure consists of voids (also called pores), which can be isolated or interconnected forming complex networks of channels, an example of this can be seen in Figure 2.14. Typically the pores are filled with air or water under ambient conditions. Depending on the material, fluids are able to enter or exit the voids and to move through the open voids [30].

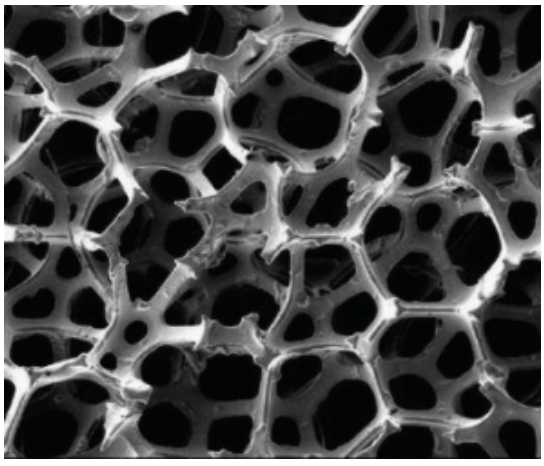

Figure 2.14: *Microstructure of a porous material [31]*

There are many characteristics of the porous media such as the total volume of void space (also called bulk porosity), void size and void distribution, the degree of inter-connectivity, roughness of voids and total surface area. Manufacturing a metallic porous structure with given parameters is a challenging task. There are three different manufacturing methods that can be used depending on the final application of the porous media.

Method 1: Metallic Foam

The first method manufactures a metallic foam. In this process a molten metal is "foamed" by injecting a gas that will decompose before the metal solidifies. It was one of the most common processes to manufacture porous media [32]. This type of porous media has very high porosity, however, it also has poor mechanical strength and long manufacturing time. This combination makes it not viable for a metallic foam to be implemented in a turbine blade.

Method 2: Lamination

The second method is called laminated porous media. In this technique multiple prefabricated layers with several etched of laser-cut micro-channels are combined by welding [33]. This type of metal porous fabrication improves the controllability of the flow and the internal heat transfer as the porosity of each layer is predetermined. The biggest disadvantage of this method is the assembly process, it is complicated and time-consuming.

Method 3: Powder Bed Fusion

The last method is metal sintering, Powder Bed Fusion process. The porosity is obtained by increasing the hatch distance[2], this results in the adjacent melt lines not fusing together which leaves unfused powder in between the melt lines. The powder is later removed creating pores. This technique allows for high porosity and higher strength as compared to method 1 [34]. However, the problem with this method is that the formation of the through pores is random and non-uniform.

The samples for this experiment were manufactured using method 3, Powder Bed Fusion.

[2] Hatch distance is the distance between the melt lines

3

Theory

Before diving into the experimental set-up, the basic theory behind the experiment should be introduced and explained. Apart from the theory behind the transient heat transfer experiment and possible methods to solve the equations that are explained in Section 3.1, this chapter will also explain the standard dimensional analysis in Section 3.2 and Duhamel's superposition principle used to correct the results in Section 3.3. The chapter will be concluded with an explanation of the Matlab's numerical solver in Section 3.4

3.1. Transient heat transfer experiment

Unlike the steady-state heat transfer, transient heat transfer is a non-steady-state transfer of energy. In this process the body's temperature keeps changing with time. Situations like this arise due to multiple factors such as a sudden change in the environment temperature or changing properties of the body.

During a forced conduction process, the heat flux (q) for a single point on a flat surface can be described as:

$$q = h\,(T_R - T_w) \tag{3.1}$$

where T_w is the local surface temperature for a single point, T_R is the reference temperature of the fluid. This temperature governs the convection from the liquid crystal coated surface and assures that heat transfer coefficient, h, keeps constant for a certain point with the independence of time and temperature difference.

When conducting a two-temperature convective experiment, there are only two temperatures: mainstream temperature and temperature of the wall. In that scenario, the reference temperature is equal to the mainstream temperature $T_R = T_M$. The local heat flux depends on the temperature difference between the wall's initial temperature and mainstream temperature. For film cooling and transpiration cooling the experiment is a three-temperature problem with the three initial temperatures: mainstream temperature, T_M, coolant temperature ,T_C, and wall temperature, T_W, as can be seen in Figure 3.1. Right after the sample, when the two flow mixes, the new temperature T_R becomes a function of mainstream temperature,T_M and coolant temperature, T_C. It is expressed as:

$$T_R = \left(1-\eta\right) T_M + \eta T_C \tag{3.2}$$

Where η is the film cooling effectiveness.

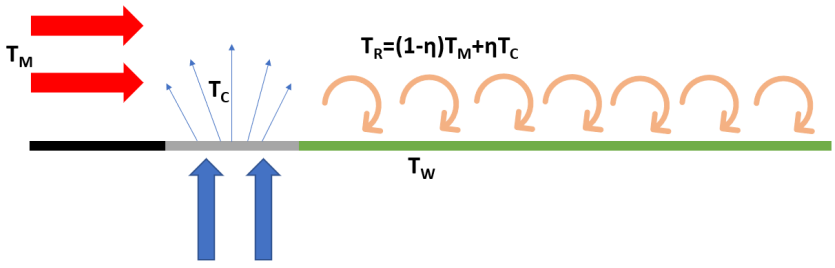

Figure 3.1: *Three-temperature problem*

Another factor to be considered is the wall material. Its properties can partially influence the experiment results. In this transient heat transfer experiment, the TLC sheet is suddenly exposed to the preheated mainstream and the ambient temperature (or preheated) coolant flow. The TLC is used as the transient wall temperature indicator. Before the mixture touches the surface, the entire solid test object is considered to have a uniform through thickness temperature, T_i. The partial differential heat conduction equation that represents this model is shown below:

$$\frac{\partial^2 T}{\partial z^2} = \frac{1}{\alpha}\frac{\partial T}{\partial t} \tag{3.3}$$

Where:

$$\alpha = \frac{\lambda}{\rho C_p} \tag{3.4}$$

Where λ is heat conductivity, ρ is density and C_p is specific heat capacity.
Implementing a semi-finite analysis to equation 3.3, one initial condition and two boundary conditions for one-dimensional transient test are obtained:

$$\lim_{z\to\infty} T(z,t) = T_i \tag{3.5}$$

$$T(z,0) = T_i \tag{3.6}$$

$$-\lambda\frac{\partial T(0,t)}{\partial z} = h(T_w - T_R) \tag{3.7}$$

Equation 3.5 assumes that the bottom plate of the test section (the plate that TLC rests upon) has an infinite boundary in through-the-thickness direction and the temperature penetration will not have any impact on the infinite boundary. In other words, the heat flux should not penetrate the thickness of the wall material resulting in no heat transfer between the fluid and the wall.

The solution described by Carslaw [35] for equations 3.3-3.7 explains a relationship among the heat transfer coefficient, the thermal properties of the wall material and time-and-position-varying wall surface temperature. The derivation can be found in the appendix A.

$$\frac{T_w - T_i}{T_R - T_i} = 1 - \exp\left[\frac{h^2\alpha t}{\lambda^2}\right]\operatorname{erfc}\left[\frac{h\sqrt{\alpha t}}{\lambda}\right] \tag{3.8}$$

$$\beta = h\sqrt{\frac{t}{\lambda\rho C_p}} \tag{3.9}$$

$$\frac{T_w - T_i}{T_R - T_i} = 1 - \exp\left[\beta^2\right]\operatorname{erfc}\left[\beta\right] \tag{3.10}$$

This solution is the general approach to solve a heat conduction problem. But film cooling and transpiration cooling are three temperatures problem as there are two different flows that are mixing. Therefore, by reorganising and combining equations 3.2, 3.8 and 3.9, a new equation is generated, in which there are two unknowns film cooling effectiveness, η, and heat transfer coefficient, h:

$$\left\{1 - \exp\left[h^2\frac{t}{\lambda\rho C_p}\right]\operatorname{erfc}\left[h\sqrt{\frac{t}{\lambda\rho C_p}}\right]\right\}\cdot\left[\eta T_C + (1-\eta)T_M - T_i\right] + T_i - T_w = 0 \tag{3.11}$$

Since there are two unknowns and one equation, it is not possible to solve this equation. There are three methods that can be used to solve this: two-peaks method, hue method and two-tests method.

Method 1: two-peaks

The method of 2 peaks requires one test. During the test two parameters are recorded t_r and t_g, which are times when the crystals reach peak red and green colour. $T_{w,r}$ and $T_{w,g}$ are calibrated temperatures from the TLC sheet. This leaves only two unknowns h and η for the two equations 3.12, 3.13, which makes the system a determined system of equations.

$$\left\{1-\exp\left[h^2\frac{t_r}{\lambda\rho C_p}\right]\operatorname{erfc}\left[h\sqrt{\frac{t_r}{\lambda\rho C_p}}\right]\right\}\cdot\left[\eta T_C+\left(1-\eta\right)T_M-T_i\right]+T_i-T_{w,r}=0 \tag{3.12}$$

$$\left\{1-\exp\left[h^2\frac{t_g}{\lambda\rho C_p}\right]\operatorname{erfc}\left[h\sqrt{\frac{t_g}{\lambda\rho C_p}}\right]\right\}\cdot\left[\eta T_C+\left(1-\eta\right)T_M-T_i\right]+T_i-T_{w,g}=0 \tag{3.13}$$

Method 2: Hue

The Hue method, is also known as temperature history matching method. It requires one test and uses the full history of the measured temperature. This provides an over-determined system of equations for obtaining η and h. For that reason, this method is very useful for steady-state experiments.

Method 3: two-tests

The last method is to use two separate tests, with the same mass flows but different coolant temperatures (while other parameters stay at the same settings), referred as the 'cold' and 'hot' test. The only difference is that, in the 'cold' test the coolant is kept at ambient temperature while in the 'hot' test the coolant is pre-heated. That means there are two equations 3.14 and 3.15, with two unknowns η and h, which means the system of equations is determined and can be solved.

$$\left\{1-\exp\left[h^2\frac{t_{g,c}}{\lambda\rho C_p}\right]\operatorname{erfc}\left[h\sqrt{\frac{t_{g,c}}{\lambda\rho C_p}}\right]\right\}\cdot\left[\eta T_{C,c}+\left(1-\eta\right)T_M-T_{i,c}\right]+T_{i,c}-T_{w,c}=0 \tag{3.14}$$

$$\left\{1-\exp\left[h^2\frac{t_{g,h}}{\lambda\rho C_p}\right]\operatorname{erfc}\left[h\sqrt{\frac{t_{g,h}}{\lambda\rho C_p}}\right]\right\}\cdot\left[\eta T_{C,h}+\left(1-\eta\right)T_M-T_{i,h}\right]+T_{i,c}-T_{w,h}=0 \tag{3.15}$$

The method of two tests is used for this experiment because it was the most suitable. For instance, it was shown by Billot [27], the two peak method was proven to be numerically unstable and the Hue method also faced issues. As explained by Li [26], there is no hue curve that would fit correctly for the whole surface of the TLC.

In ideal conditions $T_R=\eta T_C+\left(1-\eta\right)T_M$ is constant during a single transient test and the temperature at the mainstream flow loop inlet is able to achieve a step change from ambient temperature to a mainstream flow temperature. But it is not possible in reality. Instead of a step change, there is a gradual increase. To account for this the Duhamel superposition principle needs to be implemented. This principle is a general method for obtaining a solution of inhomogeneous linear evolution equations and it will be further explained in more detail in Section 3.3.

Main outputs

The experiment's main outputs are the film cooling effectiveness, η, and the heat transfer coefficient, h. These parameters will be presented on a 2D colour-maps to show downstream progression and as laterally-averaged line graphs. Additionally, heat transfer coefficients ratio, $\frac{h}{h_0}$, and heat flux ratio, $\frac{q}{q_0}$, will be produced. The h_0 and q_0 are outputs for a non-cooled experiments, with only mainstream flow loop (no coolant flow). The expression to evaluate $\frac{q}{q_0}$ is [36]:

$$\frac{q}{q_0}=\left(\frac{h}{h_0}\right)\left(1-\frac{\eta}{\phi}\right) \tag{3.16}$$

Where $\phi=\frac{T_W-T_M}{T_C-T_M}$ is the overall cooling effectiveness. Standard values for ϕ in the actual engines vary from 0.5 to 0.7[36], for this research value of $\phi=0.6$ is assumed, as the mean value of the actual range. This ratio shows how the cooling method influences the heat flux over the surface. If the value is below 1, the effect of the cooling method is beneficial.

3.2. Dimensional analysis

In engineering, dimensional analysis is the analysis of the relationships between different physical quantities by identifying their base quantities. Normally, the parameters for cooling are divided into two types: one is based on the geometry of cooling hole for film cooling, for example Reynolds Number,Re, and another type depends on the flow properties, for example blowing ratio, M. For this experiment four dimensionless quantities are used:

$$\eta = f\left(\frac{x}{D}, \frac{x}{L}, Re, M\right) \tag{3.17}$$

Geometry-based distance

For film cooling the hole diameter has effect on the downstream performance of the sample. Therefore, for easier comparison with other studies the geometry based distance, $\frac{x}{D}$ and $\frac{x}{L}$, is introduced, respectively for the film and transpiration cooling samples.

For the film cooling, it is based on the hole diameter, D, so $\frac{x}{D} = 1$ indicates the distance exactly one diameter away from the hole's edge. For the transpiration cooling it is based on its streamwise width, L. Therefore, $\frac{x}{L} = 1$ indicates distance exactly one width away from the edge of porous structure.

In Figures 3.2a and 3.2b one can see how the coordinates systems are defined for film cooling and transpiration cooling samples. For transpiration cooling, the analysis starts at $\frac{x}{L} = 2.4$ due to offset of the transpiration sample from the TLC sheet. In both figures, the red rectangle indicates Region Of Interest (ROI). This is the area that is evaluated for the final outputs. It is limited to the centre part of the TLC sheet in order to avoid any effects of the side walls of the test section might have.

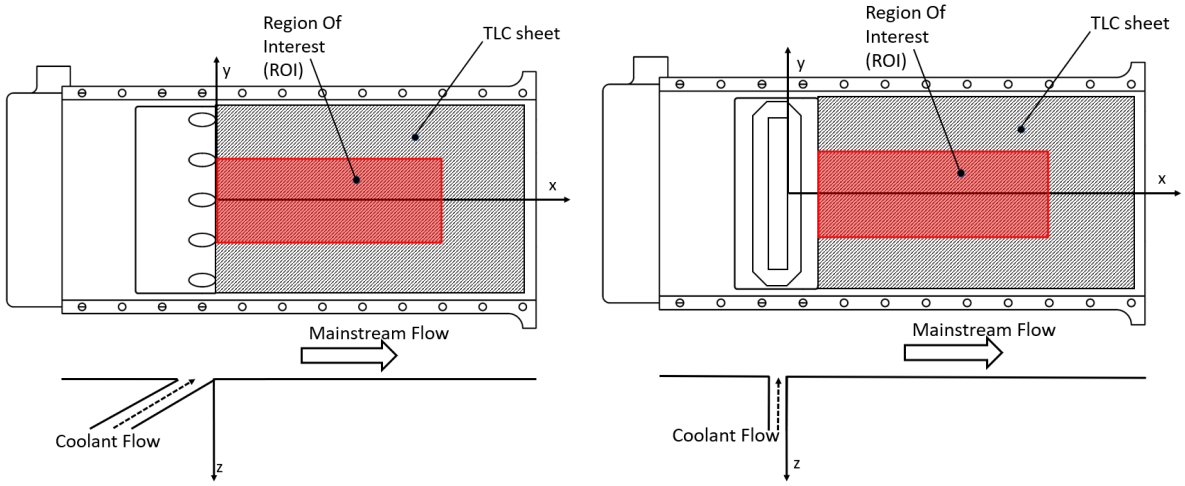

(a) *For film cooling* **(b)** *For transpiration cooling*

Figure 3.2: *2D representation of the test section*

Reynolds number

In order to be able to draw comparison between different cooling techniques the Reynolds number should be the same for both techniques. For the mainstream flow, the Reynolds number is defined and set to:

$$Re_m = \frac{v_M D_h}{\nu_M} = 25000 \tag{3.18}$$

where v_M is the flow velocity and ν_M is the kinematic viscosity of the main flow and D_h is hydraulic diameter, defined as:

$$D_h = \frac{2WH}{W+H} \tag{3.19}$$

with W and H being the width and height of the main flow rectangular cross-section, respectively.
For the coolant flow The Reynolds number is depending on the blowing ratio.
More information on the Reynolds number derivation can be found in Appendix A.

Blowing Ratio
Each sample was to be tested at different blowing ratios. The blowing ratio is defined as:

$$M = \frac{\rho_C v_C}{\rho_M v_M} \tag{3.20}$$

where ρ_C and v_C are density and velocity of the coolant flow and ρ_M and v_M are density and velocity of the mainstream flow. This equation can be simplified to:

$$M = \frac{\dot{m}_C A_M}{\dot{m}_M A_C} \tag{3.21}$$

Where $\dot{m}_C$ and A_C are the mass flow rate and the cross-section area[1] of the coolant flow loop and $\dot{m}_M$ and A_M are the mainstream mass flow rate and the cross-section area of the mainstream loop.
Since the areas of the flow channels are constant, only the mass flows can be adjusted. For this experiment, to vary the blowing ratio, the mass flow of the coolant was be adjusted. For the transpiration cooling experiments, the blowing ratio depends on the open cell porosity and pore size. The smaller pore size the higher coolant velocity. The full derivation of the blowing ratio can be found in Appendix A.

The film cooling sample was tested at several blowing ratios M=0.5, M=1, M=2. For transpiration cooling sample, the flow-through area is not known, therefore, the samples were tested at the same blowing ratio settings as film cooling sample; the same coolant mass flow rate.

Experiment time
The maximum duration of the test can be calculated as [37]:

$$t_{max} = \frac{\delta^2}{16}\frac{\rho C_p}{\lambda} \approx 200s \tag{3.22}$$

Where δ is thickness of the bottom plate of the test section.

3.3. Duhamel's superposition principle

The real-time history of the mainstream flow temperature is likely to show a continuous ramping trend due to the presence of a volume of ambient temperature in the chamber, before the hot air makes its way inside the test section, this behaviour is illustrated in Figure 3.3. As a result, the adiabatic wall temperature undergoes the following step-wise transient:

$$\Delta T_w = \left(1-\eta\right)\Delta T_M + \eta \Delta T_C \tag{3.23}$$

The mathematical adaptation of this behaviour would not be possible without Duhamel's superposition theorem. By decomposing the variation into a series of finite-step changes, the equation is rearranged:

$$T_R - T_i = \sum_{i=1}^{N} U\left(t-\tau_i\right)\Delta T_w \tag{3.24}$$

where

$$U\left(\tau-\tau_i\right) = 1 - \exp\left[\frac{h^2\alpha\left(t-\tau_i\right)}{\lambda^2}\right]\operatorname{erfc}\left[\frac{h\sqrt{\alpha\left(t-\tau_i\right)}}{\lambda}\right] \tag{3.25}$$

And the final target equation used to calculate h and η is the combination of equations 3.8 and 3.24,

$$T_R - T_i = \sum_{i=1}^{N} U\left(t-\tau_i\right)\left[\left(1-\eta\right)\Delta T_M + \eta\Delta T_C\right] \tag{3.26}$$

[1] For film cooling it is measured perpendicular to the injection angle.

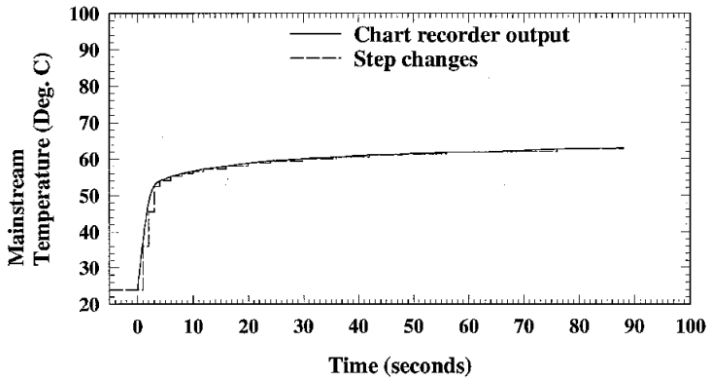

Figure 3.3: *Typical example of a mainstream temperature response during a transient heat transfer test [38]*

3.4. MATLAB solver

The goal of the solver is to solve the system of nonlinear equations 3.14 and 3.15. There are many solvers that can be implemented. The Matlab script utilises `fsolve`. The solver is used to solve the system of nonlinear equations, by changing the equation to the form of:

$$F(x) = [0] \tag{3.27}$$

Where x is a vector and $F(x)$ is a function that returns a vector value. The user can manually adjust the number of function iterations, function tolerance etc. by default `fsolve` chooses the medium-scale algorithm and uses the trust-region-dogleg method [39]. This solver is recommended because it was designed to solve non-linear system of equations.

Trust region

In a trust region algorithm the function *f(x)* is approximated with some simpler function m_k, called the model function, in the neighbourhood of x_k. The model function will not be a good approximation of *f(x)* over the entire domain, therefore, the domain needs to be restricted. It is done by setting a radius r_k centred at the point x_k, inside this radius the model function is reasonably close to *f(x)*. The name *trust region* is given because the user trusts that the model function gives a reasonably accurate approximation of *f(x)* in this region.

The model function is typically taken to be a quadratic approximation of *f(x)* based on its Taylor series expansion about the point x_k:

$$m_k(x) = f(x_k) + (x - x_k)^T \nabla f(x_k) + \frac{1}{2}(x - x_k)^T H_k (x - x_k) \tag{3.28}$$

Dogleg method

The first step of the dogleg method is to choose two directions. Typically they are chosen to be Gauss-Newton direction (equation 3.29) and the steepest descent direction (equation 3.30):

$$\delta_{gn} = -H_k^{-}1 \nabla f(x_k) \tag{3.29}$$

$$\delta_{sd} = -\frac{\nabla f(x_k)^T \nabla f(x_k)}{\nabla f(x_k)^T H_k \nabla f(x_k)} \nabla f(x_k) \tag{3.30}$$

Given a trust region with radius r_k dogleg method selects the updated step δ_k as equals:

1. If the path lies completely within the trust region the dogleg minimizer is the end point, δ_{gn}, This is the case if the Gauss-Newton step is within the trust region.

2. When the path intersects the boundary of the trust region in the first line segment, the dogleg minimiser is $\frac{r_k}{||\delta_{sd}||}\delta_{sd}$ if both the Gauss-Newton and the steepest descent steps are outside the trust region.

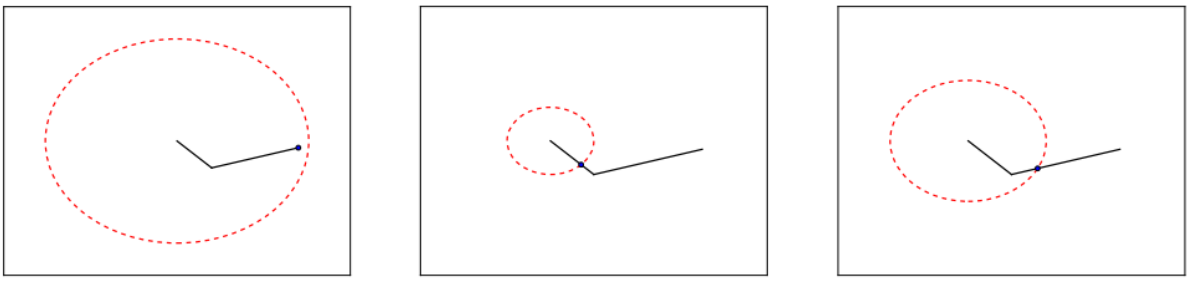

(a) *Dogleg path completely within the trust region*

(b) *Intersection in the first leg of the path*

(c) *Intersection in the second leg of the path.*

Figure 3.4: *Relationships between the dogleg path (black solid line), the trust region boundary (red dashed circle), and the dogleg minimizer (blue dot) [40]*

3. When the path intersects the boundary of the trust region in the second segment, the dogleg minimiser is given as: $\delta_{sd} + (\tau^* - 1)(\delta_{gn} - \delta_{sd})$, where τ^* satisfies the equation $||\delta_{sd} + (\tau^* - 1)(\delta_{gn} - \delta_{sd})||^2 = r_k^2$.

Solving systems of nonlinear equations
In order to solve a system of nonlinear equations $r(x)$:

$$r(x) = \begin{bmatrix} r_1(x) \\ r_2(x) \\ . \\ . \\ . \\ r_n(x) \end{bmatrix} \tag{3.31}$$

For a trust region method to find roots of a system of equations, the objective function whose minima correspond to roots of the system needs to be introduced, for example:

$$f(x) = \frac{1}{2}||r(x)||_2^2 = \frac{1}{2}\sum_{i=1}^{n} r_i(x)^2 \tag{3.32}$$

It, roughly speaking, measures how close a point x is to be a root of $r(x)$. Note that $f(x) = 0$, if and only if, $r(x) = 0$. Therefore, if a global minimum of $f(x)$ can be successfully found, the root to the nonlinear system is also found.

$$J_k = \begin{bmatrix} \nabla r_1(x_k)^T \\ \nabla r_2(x_k)^T \\ . \\ . \\ . \\ \nabla r_n(x_k)^T \end{bmatrix} \tag{3.33}$$

Then the gradient is $\nabla f(x) = J_k^T r(x_k)$and the Hessian $H_k = J_k^T J_k$. Therefore the equations 3.29 and 3.30 become:

$$\delta_{gn} = -\left(J_k^T J_k\right)^{-1} J_k^T r\left(x_k\right) \tag{3.34}$$

$$\delta_{sd} = -J_k^T r\left(x_k\right) \tag{3.35}$$

The dogleg method can be summarised in a flowchart, as seen in Figure 3.5.

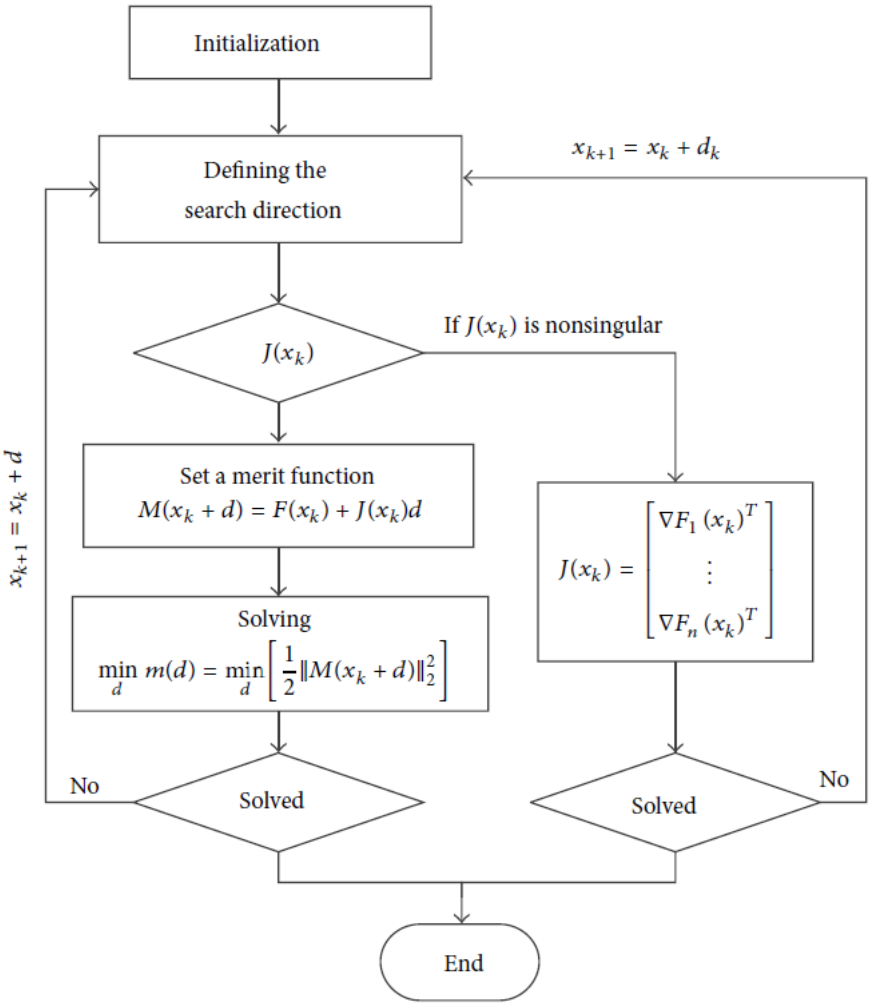

Figure 3.5: *Flow chart for trust region dogleg algorithm [41]*

4

Experiment

In this chapter the experimental set-up will be explained together with the testing procedure. This chapter is structured as follows: first the experimental set-up is explained in Section 4.1. Next, the different tests are explained in Section 4.2, subsequently in Section 4.3 data post-processing is explained. The chapter is wrapped up with explanation of how the experimental set-up was validated in Section 4.4.

4.1. Set-up

The goal of the experiment is to obtain the heat transfer coefficient and film cooling effectiveness. This requires a set-up with a number of components, which will be expained in the sections below.

4.1.1. Test rig

The test set-up can be seen in Figure 4.1. It consists of two flow loops: mainstream loop and a coolant loop. Both loops can be either directed to the test section or be bypassed to the ambient environment by means of 3-directional ball valves for the coolant loop and a hatch valve for the mainstream loop. Each loop has a separate heater and power regulating unit, allowing to alter their temperatures independently. There are multiple pressure and temperature measurement points on both flow loops.

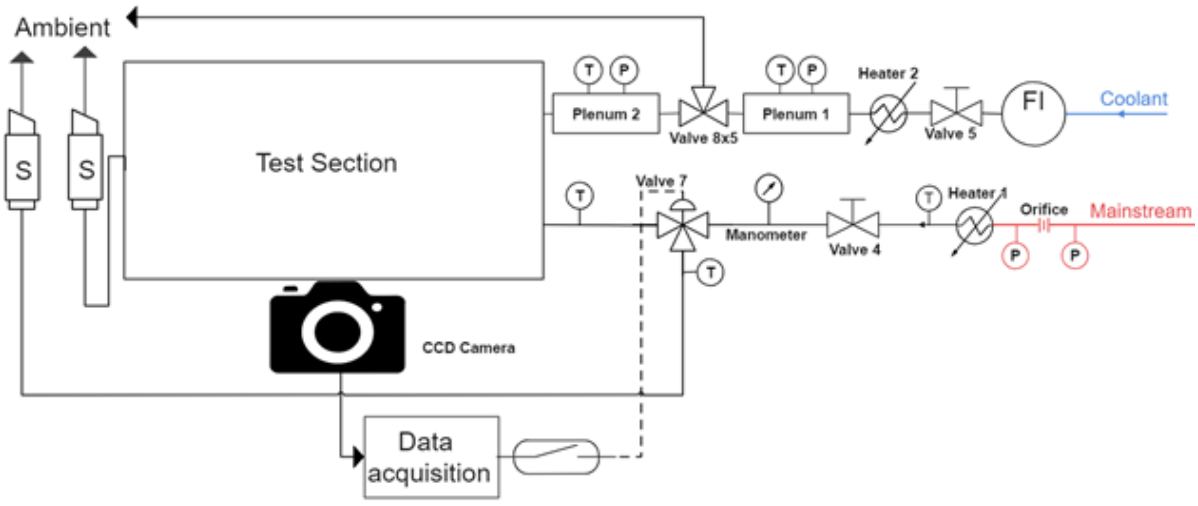

Figure 4.1: *Test rig scheme*

The mainstream loop is connected to a compressed air system operating at 8bar. The air first passes through an orifice meter, the heater and into 1.5m long rectangular pipe, with the same cross-sectional dimensions as the test section. This is done to ensure that a fully developed flow enters the test section. Next, the air can either enter the test section with cross-sectional dimensions of: 150mm by 85mm or it can be directed to the ambient environment.

The coolant loop is connected to the same compressed air system as the mainstream loop. First the air passes through the Coriolis flow meter and the heater into the plenum 1 where pressure and temperature measurements are taken. Subsequently, the flow is divided into 5 pipes which can be directed either towards the ambient environment or towards the sample. If the flow is directed towards the sample, first it reaches plenum 2, where pressure and temperature are measured right before the flow goes through the film cooling or the transpiration cooling sample to the test section.

Test section
The test section is a rectangular box with one inlet for the mainstream flow, one inlet for the coolant flow (where the film cooling or transpiration cooling sample is mounted) and one outlet. In Figure 4.2 a render of the test section together is shown. The test section is located on the left-hand side. The bottom plate of the test section is made 3d printed in PD2200 Nylon and it is flushed/aligned with the sample. On top of the bottom plate a Thermochromic Liquid Crystals sheet, with approximate dimensions of 130mm by 230mm, is placed. The side plates are made from PD2200 Nylon. The top plate of the test section is made from 16mm thick plexiglass to ensure that the camera can record the colour changes of the TLC. On top of the plexiglass there is a small LED. The LED is switched on at the beginning of the experiment in order to mark the first image from the image acquisition process.

Image acquisition set-up
One of the main issues with with image acquisition set-ups for this experiment, is light reflection of the TLC sheet, therefore the illumination source should not be placed directly above the crystals. The current configuration is making use of four fluorescent bulbs (OSRAM DULUX S, 11W, 3000K), see Figure 4.3, that are mounted on the square metal frame. In the centre of the frame, located approximately 50cm above the test section there is a CCD Blackmagic Pocket Cinema Camera. In order to reduce the amount of light dispersed to the environment, the whole structure and the camera is enclosed in black drape during the experiment. Additionally, this ensures that no light, other than from the bulbs, is affecting the image acquisition system.

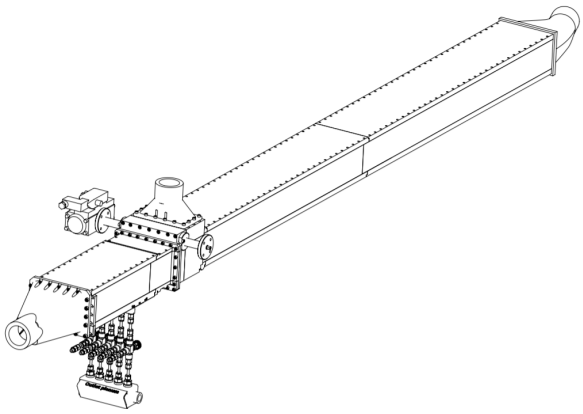

Figure 4.2: *Render of the experimental rig*

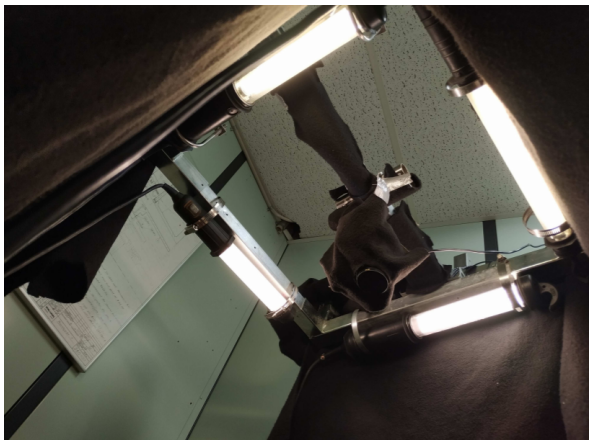

Figure 4.3: *Lighting set-up*

The current solution proved to be the least invasive; providing a symmetrical diffused light and a minimum amount of reflection on the surface [27].

Camera settings
In the Table 4.1 the camera settings are shown for this experiment. As mentioned earlier the camera is a CCD Blackmagic Pocket Cinema Camera with a resolution of 1920 x 1080 pixels. The next settings are frame rate and time lapse interval; frame rate is number of frames the camera takes in a second, whereas the time lapse interval is the setting that allows to record a still frame at some specified intervals. For this experiment a frame rate of 30 frames per second was chosen with a time lapse interval of 3 frames, this results in 10 pictures every second, or in other words one picture every 0.1second. These settings were deemed as sufficient to see the evolution of the colours in the crystals without having an extensive computational times for post-processing. As recommended by the manufacturer, for the good light conditions, optimal ISO setting was chosen to be 800. The shutter angle regulates the amount of light that reaches the sensor. As explained by Billot [27], a shutter angle of 270^o was chosen as optimal. For a white balance setting, a value of 3000K was chosen, this is to account for the lighting conditions. The white balance ensures that white colour stays white in the image.

Table 4.1: *Camera settings*

Parameter	Value
Camera type	CCD Blackmagic Pocket Cinema Camera
Picture dimensions [pixels]	1920x1080
Frame rate [fps]	30
Time lapse interval [-]	every 3 frames
ISO [-]	800
Shutter angle [^{o}]	270
White Balance [K]	3000

TLC
For this experiment, TLC sheets from Hallcrest are used. The colour play of the TLC is R35C1W which means that point Red Start is at 35^oC and the bandwidth is 1^oC. The full properties of this TLC sheet are displayed in Table 4.2.

Table 4.2: *R35C1W TLC properties [42]*

Colour play	Red Start [^oC]	Green Start [^oC]	Blue Start [^oC]	Clearing point [^oC]	Bandwidth [^oC]
R35C1W	35.0	35.2	36.0	49.0	1

For this TLC the tolerances for Red Start are $\pm 0.5^oC$ and for the bandwidth $\pm 0.2^oC$. Although the Green Start is indicated to start at 35.2^oC, each new batch of TLC needs to be calibrated for this experimental set-up. The calibration procedure for this existing set-up was described by Billot [27]. For currently used batch, the maximum intensity of the green colour, the green peak, was found to be at 34.17^oC.

4.1.2. Test object

Transpiration cooling samples were manufactured using nickel-based Hastelloy-X (batch 1) and Inconel 625 (batch 2). The chemical composition of both materials can be found in Table 4.3. Both batches were manufactured using Laser Powdered Bed Fusion method. The samples consisted of a 10mm by 110mm porous strip surrounded by a solid metal frame in an elongated hexagonal shape. The technical drawing of the sample can be found in Appendix B.

Table 4.3: *Chemical composition of Hastelloy-X and Inconel 625 [43] [44]*

Element	Hastelloy-X	Inconel 625
Nickel	47%	58% min
Chromium	22%	20-23%
Molybdenum	9%	8-10%
Iron	18%	5% max
Niobium+tantalum	0.5% max (Niobium only)	3.15-4.15%
Cobalt	1.5%	1%max
Silicon	1% max	0.5% max
Manganese	1% max	0.5% max
Titanium	0.15% max	0.4% max
Silver	-	0.4% max
Carbon	0.1%	0.1% max
Sulphur	-	0.01% max
Phosphorus	-	0.01% max
Tungsten	0.6%	-
Boron	0.008% max	-
Aluminium	0.5% max	-

The transpiration samples are numbered from 1-6, each number corresponds to a different printing parameters (e.g plate 1 from batch 1 has same printing parameters as plate 1 from batch 2). Each plate was manu-

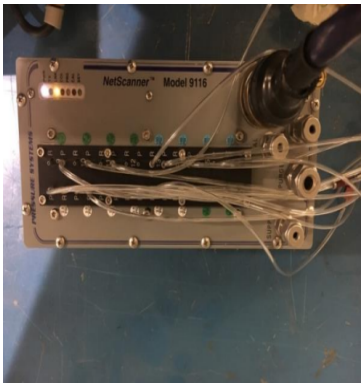

(a) *Netscanner model 9116*

(b) *Rosemount 2088*

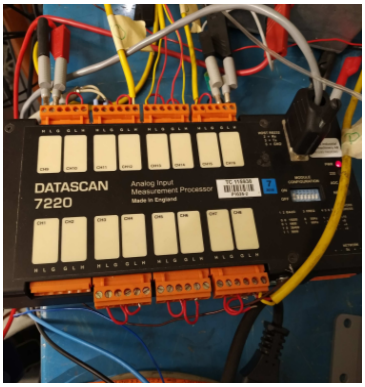

(c) *Agilent 34972A*

Figure 4.4: *Data acquisition set-up*

factured with three different thicknesses of the porous part: 0.5mm, 1mm and 2mm (e.g. there are 3 plates 1; plate 1 with 0.5mm thickness, plate 1 with 1mm thickness and plate 1 with 2mm thickness). In Table 4.4, the overview of samples tested and their nomenclature that will be used in this report is given.

Table 4.4: *Transpiration samples overview*

	Batch [-]	$t_p[mm]$	**Name** [-]
Plate 1	Batch 1	0.5	B1_P1_05mm
Plate 1	Batch 1	1	B1_P1_1mm
Plate 1	Batch 1	2	B1_P1_2mm
Plate 1	Batch 2	0.5	B2_P1_05mm
Plate 1	Batch 2	1	B2_P1_1mm
Plate 1	Batch 2	2	B2_P1_2mm
Plate 2	Batch 2	0.5	B2_P2_05mm

4.1.3. Measurement instruments and data collection

For any experimental set-up a data collection system is needed. For this purpose in-house software is used, a *RigView v3.3 gas turbine measurements and evaluation system.* It is an in-house developed software that is able to record data from various inputs and gather them into a .DIF format file. Moreover, RigView has also the possibility to display the real-time data during testing.

In this experiment there are many electronic components, the pressures are being recorded using *NetScanner Model 9116*, Figure 4.4a. The scanner features a 16 channel module with integrated silicon piezoresistive pressure sensors able to register values in the range of 1-5850kPa. The outcomes are calibrated against a *Rosemount 2088 Gage and Absolute Pressure Transmitter*, Figure 4.4b. The *Agilent 34972A Data Acquisition System* receives the signals from the thermocouples and feeds the values to the RigView software, Figure 4.4c. Additionally, there are 2 power regulating units: *Drehzahlregler DR-2000* for coolant flow, Figure 4.5, and one for the mainstream flow, Figure 4.6 and a power supply for a LED: *LABPAC B300D*, Figure 4.7.

Figure 4.5: *Power regulating unit for the coolant flow*

Figure 4.6: *Power regulating unit for the mainstream flow*

Figure 4.7: *Power supply for a LED switch*

4.2. Experimental procedure

As explained in Section 3.1, 2 tests are needed: cold and hot. Additionally, to account for conduction heat losses during the hot test, a heat loss test needs to be performed. Each sample will be tested for 4 different blowing ratios: 0.5, 1, 2 and 3.5.

Cold test

For the cold test the coolant temperature is set at ambient temperature whereas the mainstream temperature is set at 70^oC. The coolant settings change with the different blowing ratios and mainstream settings do not change. In Table 4.5 one can look for the settings of the cold test's campaign.

Table 4.5: *Cold test settings*

	Mainstream	**Coolant**			
	M=0.5, 1, 2, 3.5	M=0.5	M=1	M=2	M=3.5
T[^oC]	70	21.7			
$\dot{m}$[g/s]	65	0.85	1.7	3.4	6

Hot test

In the two tests method, for the hot test the the coolant temperature needs to be the same as mainstream temperature, 70^oC, [45]. In table 4.6 one can look up settings for the hot tests. Mainstream settings stay the same for all the blowing ratios.

Table 4.6: *Hot test settings*

	Mainstream	**Coolant**			
	M=0.5, 1, 2, 3.5	M=0.5	M=1	M=2	M=3.5
T[^oC]	70	70			
$\dot{m}$[g/s]	65	0.85	1.7	3.4	6

Heat loss test

During the hot test, heat from the coolant is exchanged with the plenum walls and the transpiration sample. Which means that coolant temperature above the sample is lower than the temperature measured below the sample. Since it is not possible to measure the temperature above the sample during the hot test, a heat loss test is introduced. During this test a special component attaches on top of the transpiration sample (Figure 4.8). It has 3x29 square grid that is placed over the porous part of the sample to evenly divide the coolant air. It has 5 openings for a thermocouple at a mid-line, +/-2.5cm and +/-5.5cm from the mid-line. When the thermocouple is inserted, it is located slightly above the surface of the porous strip. Together with the thermocouple in the plenum 2, they measure the temperature of the coolant flow before it enters the sample and right after it passes through the sample. Afterwards, the difference between the temperatures is implemented in the post-processing. The heat loss test is carried out at the same coolant parameters as the hot test.

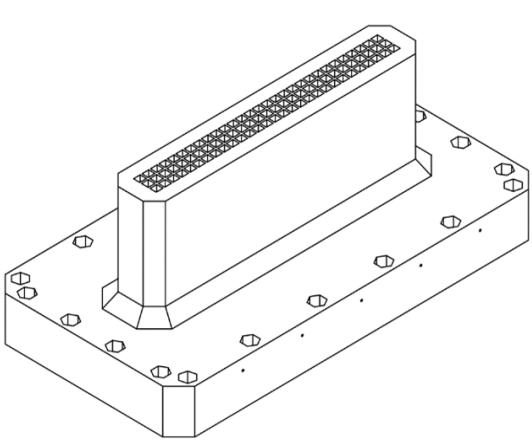

(a) *Heat loss component design*

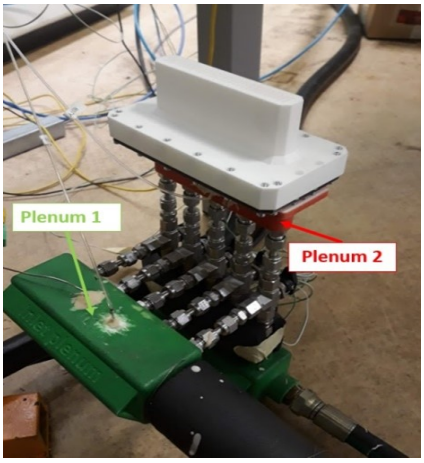

(b) *Heat loss component during testing*

Figure 4.8: *Heat loss component*

4.3. Post-processing

This experiment is a data-intensive process. In order to better manage the data, Matlab code will be utilised. The post-processing is divided into two phases to simplify the process.

First phase

The first phase of the post processing is image processing. The aim of the process is to obtain the time it took to reach a green peak intensity for each pixel. The processing goes as follow

1. Collect the information from the camera (photographs) and data scanner.
2. Import .DNG images into Matlab
3. Select of Region Of Interest (ROI)
4. Transfer the ROI from .DNG to .MAT
5. Calculate the time it needs to reach green peak intensity for each pixel

The first step of the post-process is to collect required data from various devices. The .RAW images coming from the camera cannot be processed directly by Matlab, therefore all of them need to be converted by Adobe DNG Converter. It converts the .RAW format files to .DNG (Digital Negative) format. While converting the formats the image stays uncompressed(Lossless conversion). For clarity purposes, in this document .RAW refers to a file format and raw to unprocessed pixel values which are direct output of the imaging sensor of a camera. Next step is to choose ROI. This limits the area that will be evaluated, reducing the computational time.

Step 4 is essential in the post processing. It converts the the ROI from the .DNG file to a matlab viewable output. According to (Sumner,2014) the raw image needs to be linearized, white balanced, demosaiced and colour space corrected. The last step of brightness and colour control is not needed as it is an aesthetic step to make the image more readable. Figure 4.9 sums up the workflow of transferring raw sensor data. Below is an example of image processing step by step and how it changes the MATLAB output display.

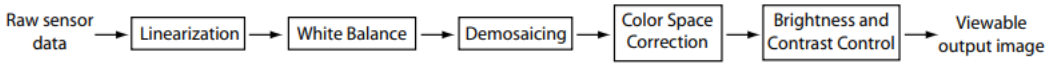

Figure 4.9: *Workflow of converting raw images [46]*

Figure 4.10a shows the raw data from the camera's sensor, which is not visible by the human eye. It is a single channel intensity image which has a non-zero minimum value to represents 'black' with integer values that contain 10-14 bits of data [46]. In Figure 4.10b the linearized image is display, the linearisation process maps

the raw values to real values between 0-1. Figure 4.10c shows white balanced image. The process of white balancing is removing unrealistic color casts, so that objects which appear white in real life are rendered white in the image. In this process each colour channel in the colour filter array (CFA) is scaled by appropriate amount to white balance the image. In order to obtain next image, Figure 4.10d, the demosiacing algorithm needs to reconstruct a full RGB colour image. One can notice that the red LED in the bottom left corner changed colour to red. Although this image is already viewable with standard MATLAB display functions. The pixels do not have coordinates in the correct RGB space that is expected by the operating system. In order to correct them a linear transformation needs to be applied, with the results visible in 4.10e. Once the image is colour space corrected it is in the right colour space for display. However it is still a linear image with values relating to what was sensed, which may not be in a range appropriate for being displayed [46]. The pixels have now correct values and these values are used in later stage of post-processing. Next two steps are simply tweaking the image so it looks appealing. In Figure 4.10f the image was brightened and in Figure 4.10g it is transformed non-linearly with a power function. In Figure 4.10h is the same image as viewed by the default photos app on the windows computer.

The last step in this part of post-processing is calculation of time needed to reach green peak for each pixel. The code takes the same pixel from each image, determines its RGB colour intensities and stores it in the matrix. Later a 21-parameter Gaussian curve s is fitted to the data. Matlab determines the frame number when the maximum green intensity is reached (the peak of the Gaussian curve) and converts it to time, which can be computed using the frame rate at which the experiment was carried out. Then the process is repeated for all the pixels.

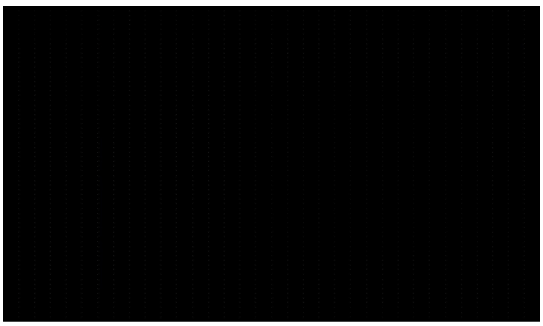

(a) *Raw sensor data*

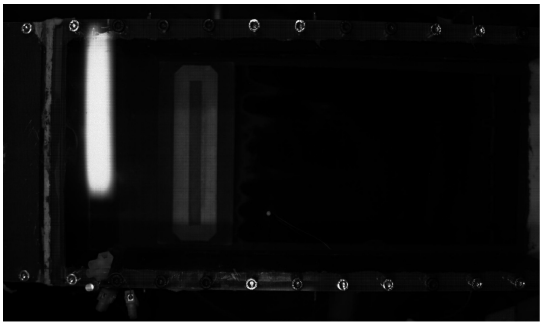

(b) *Linearized image*

(c) *White balanced image*

(d) *Demosaiced image*

(e) *Colour space corrected image*

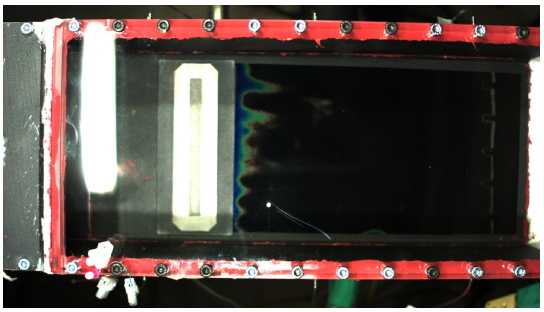

(f) *Brightened image*

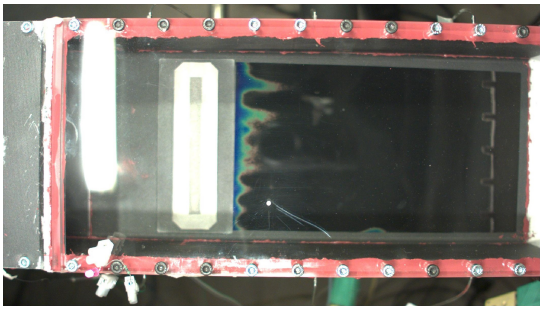

(g) *Gamma corrected*

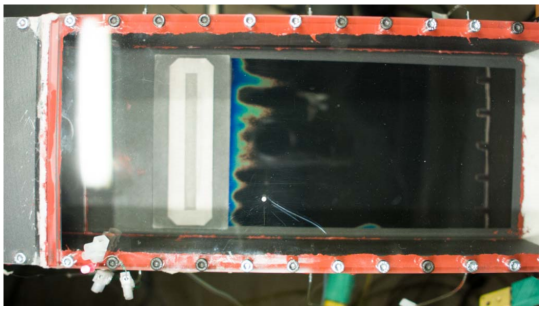

(h) *Image as displayed by computer*

Figure 4.10: *Image processing*

Second phase

Once both tests, cold and hot, were processed, second phase of post processing can take place. The aim of the second phase is to solve the system of equations. The output of this part is the heat transfer coefficient and film cooling effectiveness. The solver has following steps:

1. Import required matrices into Matlab
2. Input corresponding temperatures from the tests

3. Solve for η and h
4. Plot graphs

The first step is inputting required matrices into the Matlab workspace: $t_{g,c}$ and $t_{g,h}$. Next, corresponding temperatures need to be inputted such as initial temperature of the hot test. Next, the solver calculates the film cooling effectiveness and heat transfer coefficient using the method described in Section 3.4 and plots the colour-maps and 2-d graphs. Figure 4.11 visualises the flow processing of the data. First phase corresponds to the blue box: image processing and the second phase corresponds to the grey box: Heat transfer transient test.

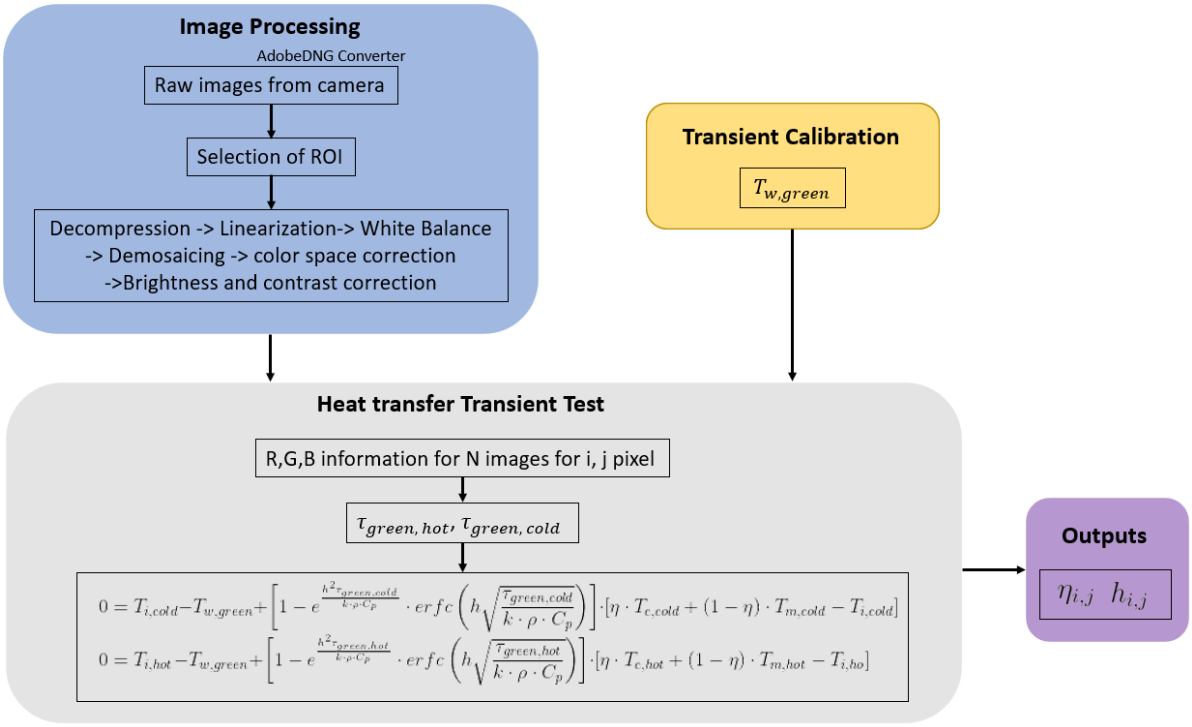

Figure 4.11: *Block diagram for the post-processing*

4.4. Rig validation

Since the transpiration cooling is a new, state-of-the-art technology there are not enough experimental results to verify the values. Therefore, the experimental setup was verified using a film cooling sample [34]. The film cooling sample was tested for three different blowing ratios, M=0.5, M=1 and M=2. In Tables 4.7, 4.8 and 4.9, flow characteristics from different validation papers are listed for blowing ratio M=0.5, 1 and 2 respectively, where the M is a blowing ratio, P is the density ratio, S/D is the distance between holes/hole diameter and $angle$ is the injection angle.

Rig Validation M=1

In Figure 4.12b, laterally averaged film cooling effectiveness for blowing ratio M=1 is compared to values obtained from different validation papers, see Table 4.7. The values from present study follow the same trend as results from other studies. There is a peak of $\bar{\eta} = 0.17$ at about $\frac{x}{D} = 3.5$ from the holes and gradually decreasing downstream. The trend line is between maximum and minimum trend lines from other papers.

In Figure 4.12a ratio of $\bar{h}$, laterally averaged heat transfer coefficient, to h_o, heat transfer coefficient obtained for a test without coolant, for blowing ratio M=1 is compared to other validation papers. The values from this study follows the general trend with peak at around $\frac{x}{D} = 1$ from the hole and beyond that the effectiveness is gradually decreasing downstream. The peak at $\frac{x}{D} = 14$ is associated with corrupted data and should be disregarded.

Table 4.7: *Flow characteristics for other studies with Blowing Ratio, M=1, adapted from [34]*

Study	$\bar{h}/ho$				$\bar{\eta}$			
	M	P	S/D	angle	M	P	S/D	angle
Present study	1	1.1	3	30	1	1.1	3	30
Wright et al. 2010 [47]	-	-	-	-	1	1	4	35
Dhungel et al. 2007 [48]	1	-	-	30	1	-	-	30
Baldauf et al. 2002 [49],[50]	1	1.2	3	30	1	1.2	3	30
Yu et al. 2002 [36]	1	0.9-1.1	-	30	1	0.9-1.1		30
Nasir et al. 2001 [51]	1.13	1	-	35	1.13	1	-	-
Gritsch et al. 1998 [52]	1	-	-	-	-	1.5	-	-
Goldstein et al. 1998 [53]	1	1	-	35	-	-	-	-
Schmidt et al. 1994 [54]	-	-	-	-	-	1.25	-	-
Ammari et al. 1990 [55]	1	1	3	35	-	-	-	-
Hay et al. 1985 [56]	1	1	3	35	-	-	-	-
Pedersen et al. 1977 [57]	-	-	-	-	-	-	0.96	-
Eriksen and Goldstein 1974 [58]	1	1	3	35	-	-	-	-

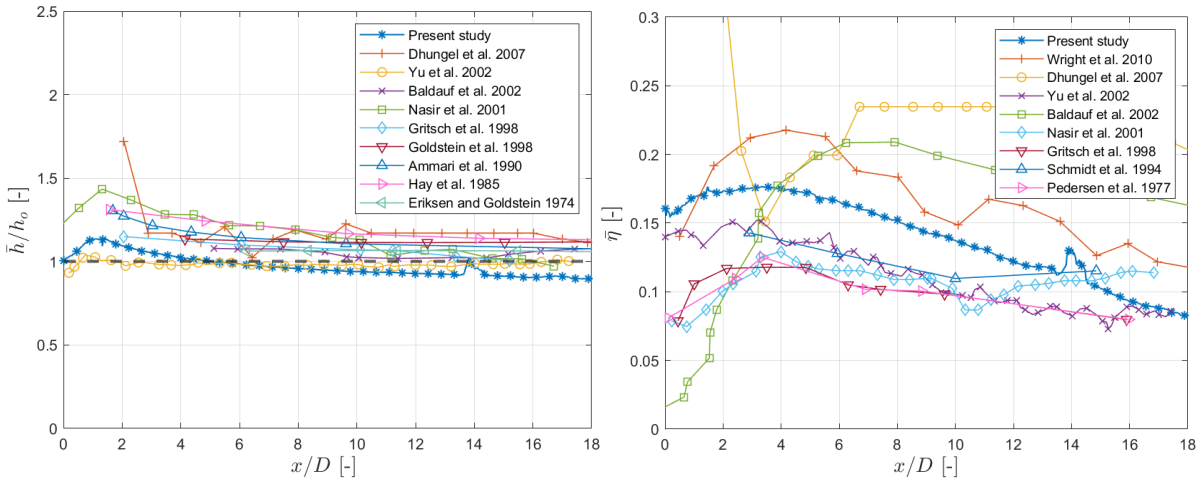

(a) *Ratio of Heat transfer coefficient Laterally Averaged* **(b)** *Film Cooling Effectiveness Laterally Averaged*

Figure 4.12: *Rig validation for blowing ratio M=1, adapted from [34]*

Rig Validation M=0.5

In Figure 4.13b, laterally averaged film cooling effectiveness is shown. Performance at the blowing ratio M=0.5 follows the same trend as most of the studies, with a peak cooling effectiveness,$\bar{\eta} = 0.35$ at around $\frac{x}{D} = 4$ and a steady decrease until $\frac{x}{D} = 18$. The trend line for this study is within the trend lines obtained from other studies.

Table 4.8: *Flow characteristics for other studies with Blowing Ratio, M=0.5,adapted from [34]*

Study	$\bar{h}/ho$				$\bar{\eta}$			
	M	P	S/D	angle	M	P	S/D	angle
Present study	0.5	-	3	30	0.5	-	3	30
Wright et al. 2010 [47]	-	-	-	-	0.5	-	3	30
Dhungel et al. 2007 [48]	0.5	-	-	30	0.5	-	-	30
Yu et al. 2002 [36]	0.5	-	-	30	0.5	-	3	30
Baldauf et al. 2002 [49],[50]	0.5	1.8	3	30	-	-	-	-

In Figure 4.13a, ratio $\frac{\bar{h}}{h_o}$ for blowing ratio M=0.5 is compared to results from other validation papers. At first,

the trend line steadily increases to about $\frac{\bar{h}}{h_o} = 1.2$ at about $\frac{x}{D} = 5.5$ and then the trend line decreases slowly to about $\frac{\bar{h}}{h_o} = 1.1$ in the region further downstream. Although, the values from present study have the highest ratio across the evaluated span, the trend is the same as for all other studies. The peaks at $\frac{x}{D} = 1.8$, $\frac{x}{D} = 14.1$, $\frac{x}{D} = 15$ are associated with corrupted data and should be disregarded.

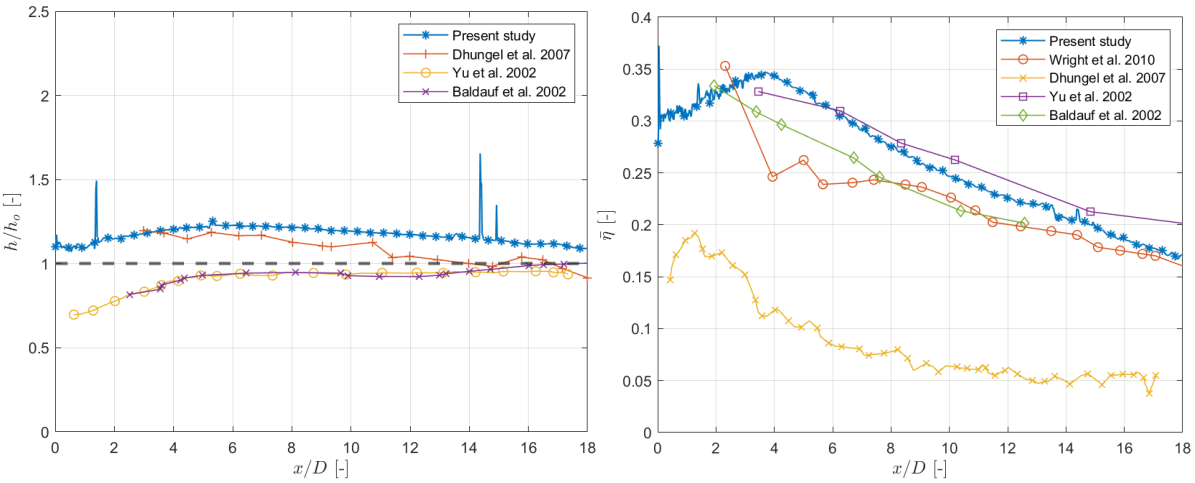

(a) *Ratio of Heat transfer coefficient Laterally Averaged*

(b) *Film Cooling Effectiveness Laterally Averaged*

Figure 4.13: *Rig validation for blowing ratio M=0.5, adapted from [34]*

Rig Validation M=2

In Figure 4.14b, laterally averaged film cooling effectiveness for blowing ratio M=2 is shown against the results from other studies. Once again, $\bar{\eta}$ follows the trend from other studies. In the first region right after the sample, the averaged performance decreases to around $\bar{\eta} = 0.075$. Later, the performance improves, $\bar{\eta}$ increases to a value $\bar{\eta} = 0.11$ at about $\frac{x}{D} = 5$, and it slowly and steadily diminishes and settles at $\bar{\eta} = 0.1$.

In Figure 4.14a ratio $\frac{\bar{h}}{h_o}$ for blowing ratio M=2 is compared to other results from validation papers. The ratio starts of at around $\frac{\bar{h}}{h_o} = 1.25$ and decreases to about $\frac{\bar{h}}{h_o} = 1$ in the region further downstream. Once again, the ratio is within the trend lines obtained from other studies

Table 4.9: *Flow characteristics for other studies with Blowing Ratio, M=2*

Study	h/ho				η			
	M	P	S/D	angle	M	P	S/D	angle
Present study	2	-	3	30	2	-	3	30
Wright et al. 2010 [47]	-	-	-	-	2	1.4	-	35
Dhungel et al. 2007 [48]	2	-	3	30	2	-	3	30
Baldauf et al. 2002 [49],[50]	2	1.2	3	30	2	1.8	3	30
Goldstein et al. 1998 [53]	2	1	-	35	-	-	-	-
Ammari et al. 1990 [55]	2	1	-	30	-	-	-	-
Hay et al. 1985 [56]	2	1	-	35	-	-	-	-
Eriksen and Goldstein 1974 [58]	2	1	-	35	-	-	-	-

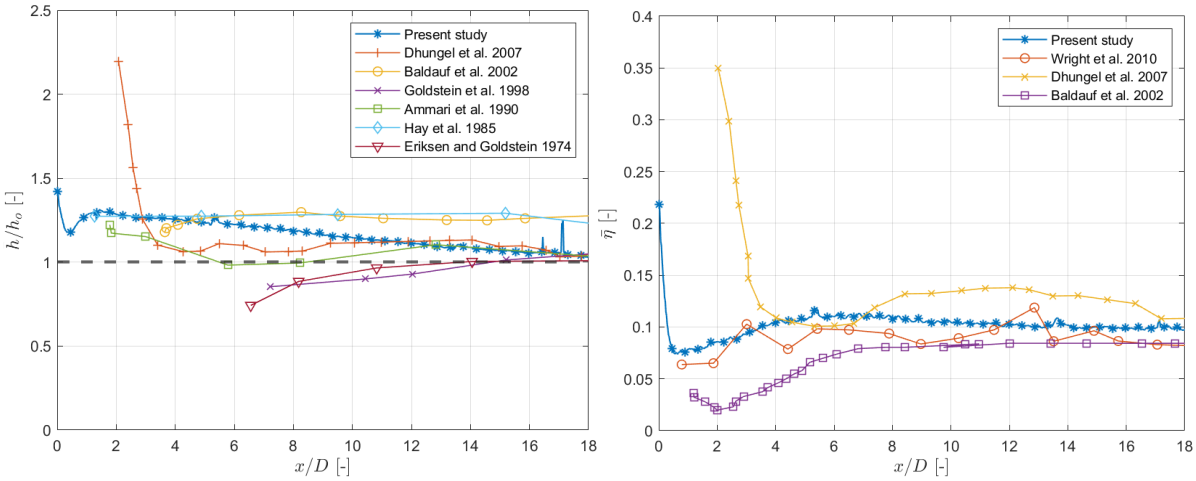

(a) *Ratio of Heat transfer coefficient Laterally Averaged*

(b) *Film Cooling Effectiveness Laterally Averaged for*

Figure 4.14: *Rig validation for blowing ratio M=2, adapted from [34]*

Figures 4.12, 4.13 and 4.14, prove that the experimental set-up and the post-processing gives results similar to the results from other published studies. Therefore, the rig can be used to test transpiration cooling samples.

5
Results

This chapter contains the results of the experiments conducted. The results are divided into three different sections. Starting with heat transfer results in Section 5.1, followed by the results from the water visualisation rig in Section 5.2. The Chapter is concluded with the performance comparison between film cooling and transpiration cooling presented in Section 5.3.

5.1. Heat transfer results

Heat transfer results were obtained using the heat transfer rig described in the Chapter 4. During post-processing two parameters were obtained: film cooling effectiveness and heat transfer coefficient. First, the results for plates 1 from batch 1 with different thicknesses are shown, followed by results for plates 1 from batch 2. Then plates B2_P1_05mm and B2_P2_05mm. Finally the corresponding plates from both batches are compared.

Batch 1

Results for the film cooling effectiveness for batch 1 are shown in the Figure 5.1. The results can be divided into 2 graphs to clearly show different trends. In Figure 5.1a results for lower blowing ratios, M=0.5 and M=1, are presented. The results in Figure 5.1 show a decreasing linear trend from the beginning. However, the average film cooling effectiveness for blowing ratio M=1 is higher than for blowing ratio M=0.5. The thickness of the porous structure had only local influence on the film cooling effectiveness. In the Figure 5.1b results for high blowing ratios, M=2 and M=3.5, are shown. The trends for these blowing ratios show an initial increase, followed by a linear decrease in the region $6 < \frac{x}{L} < 10$. Results for higher blowing ratios started to converge around $\frac{x}{L} = 10$. In the initial region results for blowing ratio M=2 were higher than the results for the blowing ratio M=3.5.

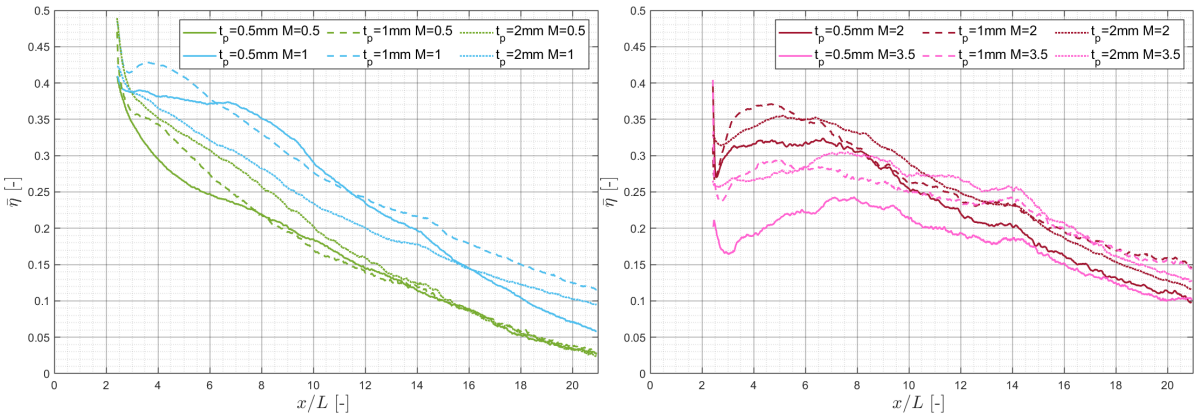

(a) *Blowing ratios M=0.5 and M=1*

(b) *Blowing ratios M=2 and M=3.5*

Figure 5.1: *Film Cooling Effectiveness Laterally Averaged for Batch 1*

As shown in Figure 5.2, the laterally averaged heat transfer coefficient depends mostly on the blowing ratio. If the blowing ratio increases the average $\bar{h}$ also increases. Apart from the results for the lowest blowing ratio, M=0.5, all the results tend to have a peak that is shifting downstream with an increasing blowing ratio. In Figure 5.3 the laterally averaged heat flux ratio is shown. Only the lower blowing ratios, M=0.5 and M=1, are below $\frac{\bar{q}}{q_0} = 1$.

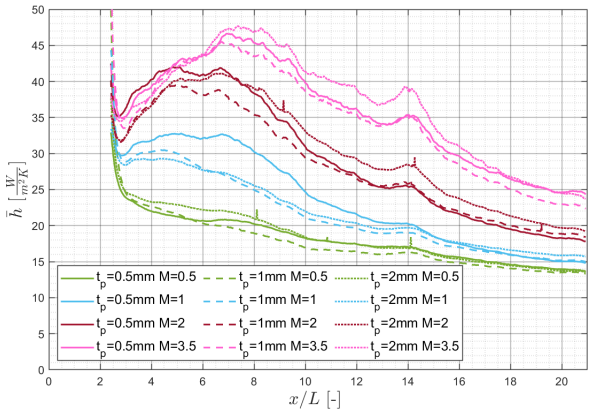

Figure 5.2: *Heat Transfer Coefficient Laterally Averaged for Batch 1*

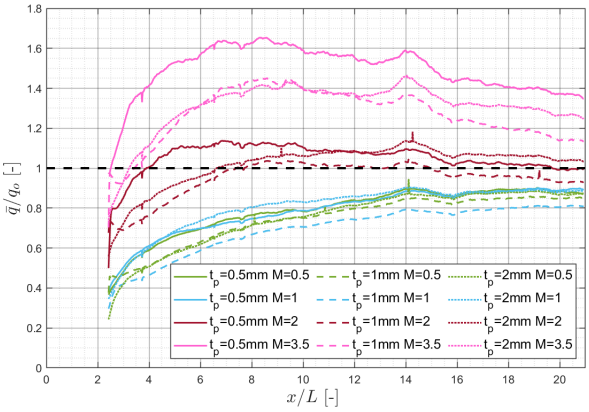

Figure 5.3: *Heat Flux Ratio Laterally Averaged for Batch 1*

Batch 2

Batch 2 was manufactured using a different material, Inconel 625, as opposed to Hastelloy-X used for Batch 1. The results for laterally averaged film cooling effectiveness are shown in Figures 5.4a and 5.4b. Similarly to batch 1, the results were grouped into two different graphs, for low blowing ratios, M=0.5 and M=1, and high blowing ratios, M=2 and M=3.5. For the low blowing ratios, the trends are linearly decreasing, whereas for the high blowing ratios, there is an initial increase or a nearly horizontal trend, followed by a linear decrease in the downstream region between $4 < \frac{x}{L} < 8$.

Results for the laterally averaged heat transfer coefficient for batch 2 are shown in the Figure 5.5. Similarly to batch 1, the average values for laterally averaged heat transfer coefficient are increasing with an increasing blowing ratio. Yet again, apart from the lowest blowing ratio, M=0.5, the laterally averaged heat transfer coefficient has a maximum value that is shifting downstream with an increasing blowing ratio. The thickness of the porous structure seems to have little to no influence on the global trends. For the laterally averaged heat flux ratio, only lower blowing ratios stay below the line $\frac{\bar{q}}{q_0} = 1$, meaning that, just like in batch 1, only these blowing ratios are beneficial to the overall cooling performance.

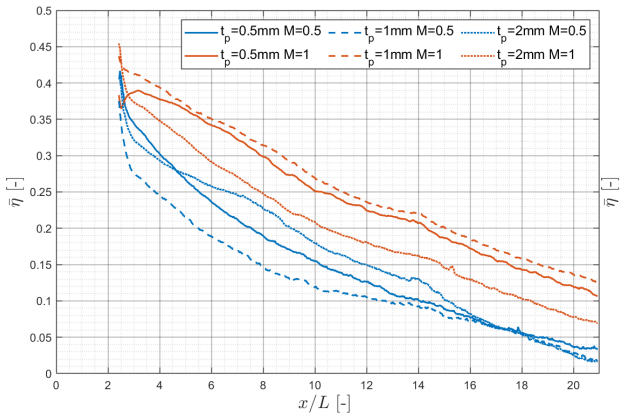

(a) *Blowing ratios M=0.5 and M=1*

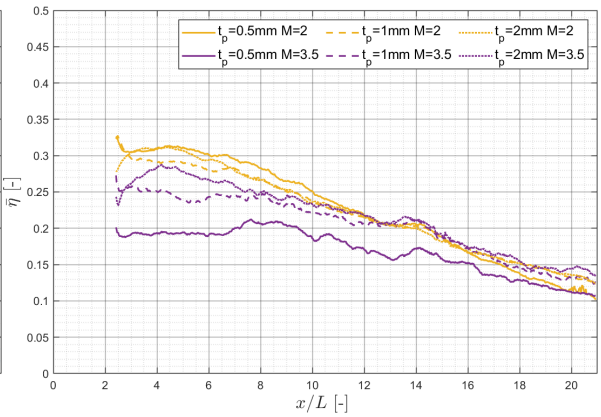

(b) *Blowing ratios M=2 and M=3.5*

Figure 5.4: *Film cooling effectiveness laterally averaged for batch 2*

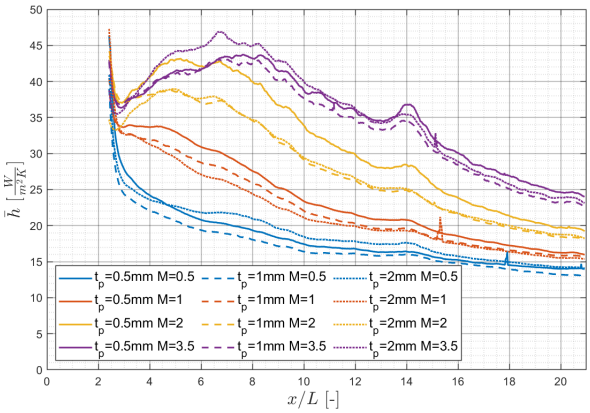

Figure 5.5: *Heat transfer coefficient laterally averaged for batch 2*

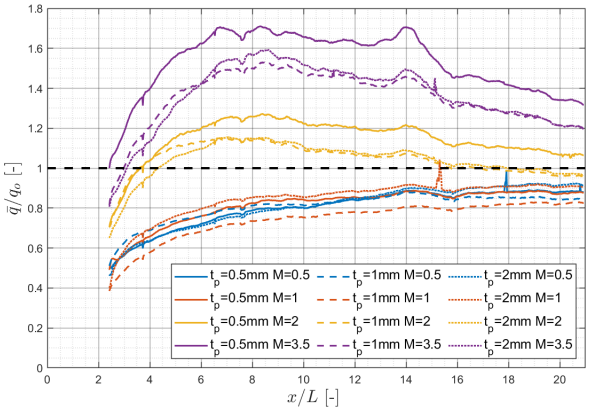

Figure 5.6: *Heat flux ratio laterally averaged for batch 2*

Comparison: different flow through areas

In this section comparison between two plates with different flow-through areas is shown. The difference in the flow through areas was explored in the water visualisation rig described in the Section 5.2 and via microscopy analysis. The microscopy investigation helped to understand the through-pore sizes, their distributions and the flow through area. In the figure 5.7a and 5.7b comparison of plates B2_P1_05mm and B2_P2_05mm is shown. Samples were manufactured using different printing dimensions but have same thickness of the porous structure[1]. In Figure 5.7a there are more light spots indicating the through-pores. These pores vary in shape and dimensions, they are not perfectly circular. Whereas in Figure 5.7b there is much less through-pores, therefore less flow-through area. This proves that different printing parameters will results in vastly different porous structures.

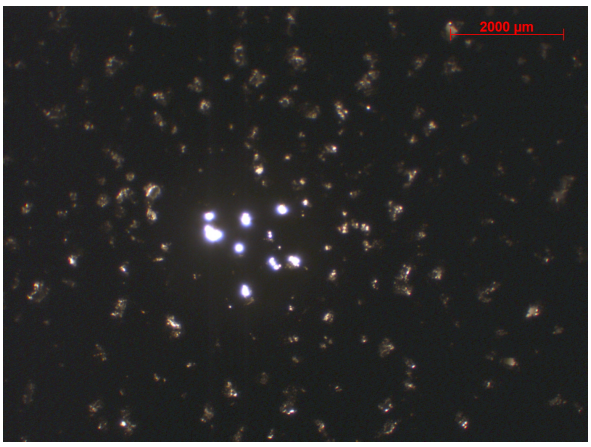

(a) *Microscopy picture for the sample B2_P1_05mm*

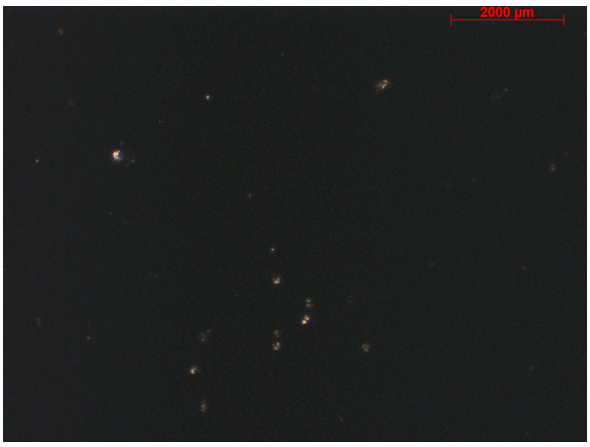

(b) *Microscopy picture for the sample B2_P2_05mm*

Figure 5.7: *Microscopy results*

The results from water visualisation rig and microscopy investigation confirmed that Plate 2, B2_P2_05mm, has smaller through flow area than plate 1, B2_P1_05mm, while having the same thickness of the porous structure.

In Figure 5.8 results for film cooling effectiveness for both of the samples are presented. For plate 2, with lower flow through area, the results at each blowing ratio are lower than for plate 1. For plate 2 all the lines follow the same trend, there is an initial increase followed by a steep decrease at between $5 < \frac{x}{L} < 8$. Interestingly, all these results converge at about $\frac{x}{L} = 10$.

[1]The brighter area in the figure 5.7a is associated with the light being located exactly behind that spot. However, all the areas that have lighter shade are through pores

In Figure 5.9 results for heat transfer coefficient are presented. For each blowing ratio plate 2, the one with a smaller flow through area, has shown an increase in laterally averaged heat transfer coefficient. Since both parameters, heat transfer coefficient and film cooling effectiveness had been adversely affected by the decrease in the flow through area, the heat flux ratio was also adversely affected. None of the results for plate 2 were below line $\frac{\bar{q}}{q_0} = 1$, which can be seen in Figure 5.10. Therefore, none of the tested blowing ratio was proven to be beneficial for the overall cooling performance.

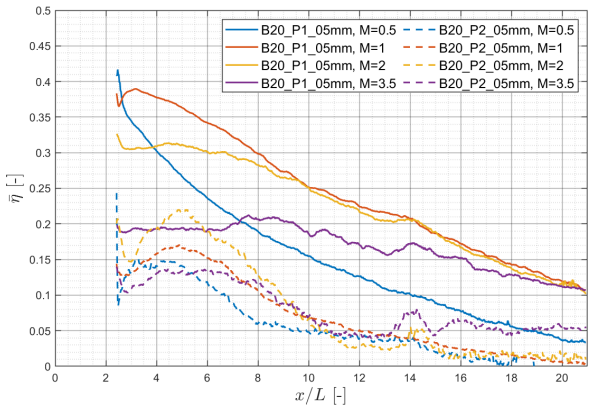

Figure 5.8: *Film cooling effectiveness laterally averaged sample B2_P1_05mm vs. sample B2_P1_05mm*

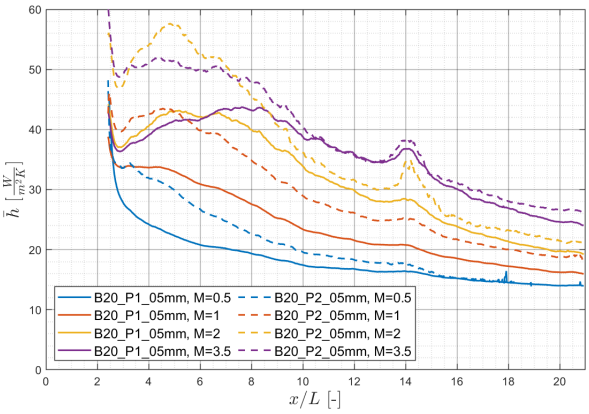

Figure 5.9: *Heat transfer coefficient laterally averaged sample B2_P1_05mm vs. sample B2_P1_05mm*

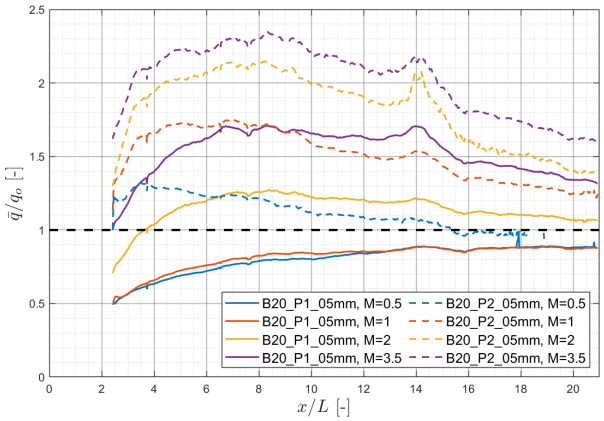

Figure 5.10: *Heat flux ratio laterally averaged sample B2_P1_05mm vs. sample B2_P1_05mm*

Combined analysis: Batch 1 vs. Batch 2

Both materials performed similarly in terms of general trends. To complete the analysis, both batches are compared within this section. Due to the similar performance, only the comparison of samples with 1mm thickness will be shown here. Comparison of samples with 0.5mm and 2mm thickness can be found in the Appendix C. For all the samples, the values were calculated using batch 1 as a reference baseline, according to the Equation 5.1.

$$\Delta\% = \frac{Batch2 - Batch1}{Batch1} \cdot 100\% \tag{5.1}$$

In Figure 5.11 laterally averaged film cooling effectiveness for samples with 1mm thickness is shown. For all the blowing ratios (with an exception of a far downstream blowing ratio M=1), batch 1 had higher values than batch 2. For the blowing ratio M=0.5, the difference between 2 batches is the largest. Performance for blowing ratio M=1 is the most similar for both batches. Whereas the differences for blowing ratio M=2 and M=3.5 are the most stable. They fluctuate between -10% and -20%.

In Figure 5.12 laterally averaged heat transfer coefficient for samples with 1mm thickness is shown. For all the blowing ratios, with an exception for blowing ratio M=1, batch 1 had slightly higher values of heat transfer

coefficient. All the differences are constant in the streamwise direction, ranging between 0% and −5% (or 0% and 5% for blowing ratio M=1).

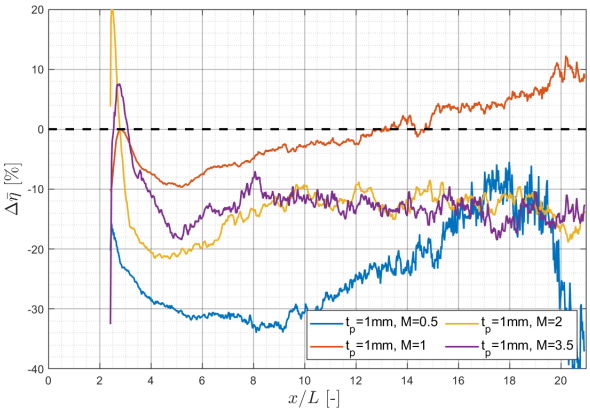

Figure 5.11: *Batch 1 vs. Batch 2: Film cooling effectiveness laterally averaged - sample 1mm*

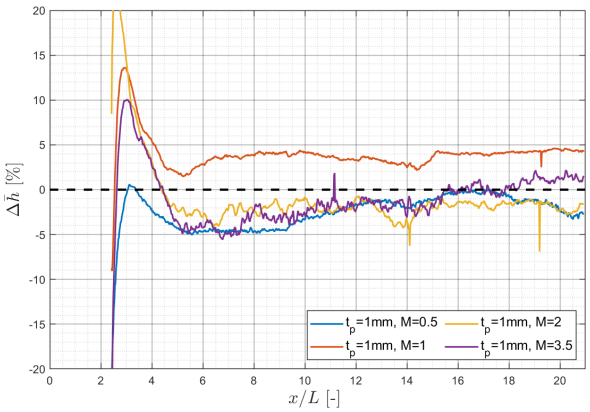

Figure 5.12: *Batch 1 vs. Batch 2: heat transfer coefficient laterally averaged - sample 1mm*

5.2. Water visualisation

The water visualisation rig was used to investigate the distribution uniformity and the directionality of the through-pores in the samples. The results for plates B1_P1_05mm, B1_P1_1mm and B1_P1_2mm are shown in Figures 5.13, 5.14 and 5.15 respectively. It is visible from the pictures that the through pores are uniformly distributed for these samples, however, there are some local variations that occur with increasing thickness of the porous structure. This non-uniformity can be seen in the figure 5.15, where there is a small gap between the water jets.

Figure 5.13: *Water visualisation for sample B1_P1_05mm*

Figure 5.14: *Water visualisation for sample B1_P1_1mm*

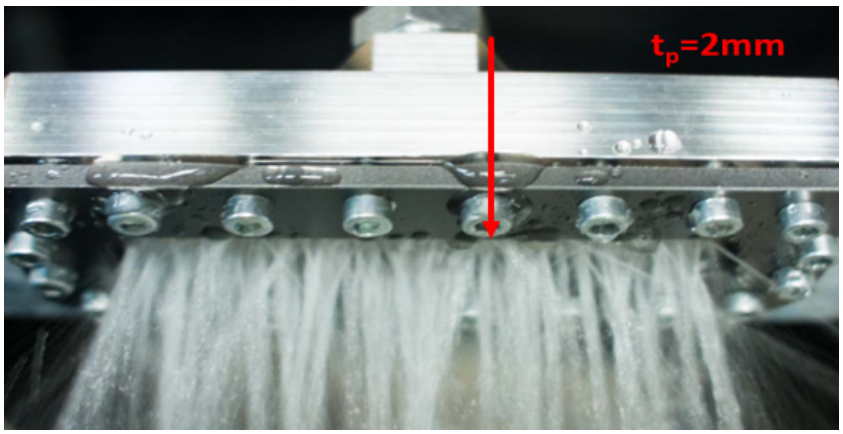

Figure 5.15: *Water visualisation for sample B1_P1_2mm*

In figures 5.16, 5.17 and 5.18 results for samples B2_P1_05mm, B2_P1_1mm and B2_P1_2mm, respectively, are visible. Here, similar trends as in batch 1 are noticeable, distributions of the through pores are uniform for samples B2_P1_05mm and B2_P1_1mm. However, in sample B2_P1_2mm there is a gap formed in the middle of the sample. This gap will have local influence on the heat transfer coefficient and film cooling effectiveness, as no coolant air can be injected through that area. This might suggest that higher thickness of the porous structure can have a negative impact on the distribution of the through pores.

Figure 5.16: *Water visualisation for sample B2_P1_05mm*

Figure 5.17: *Water visualisation for sample B2_P1_1mm*

Figure 5.18: *Water visualisation for sample B2_P1_2mm*

The difference between sample B2_P2_05mm and B1_P1_05mm is the through flow area. Sample B2_P2_05mm has a smaller flow through area. In the water visualisation rig this is displayed as many separate water jets, that do not combine together into bigger water stream when they exit the sample, see figure 5.19.

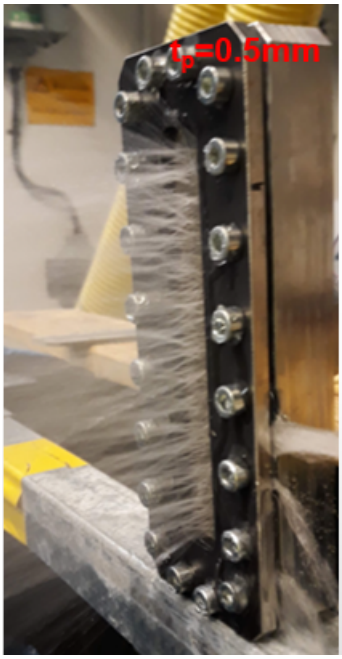

Figure 5.19: *Water visualisation for sample B2_P2_05mm*

5.3. Transpiration cooling vs. Film cooling

In order to determine whether transpiration cooling is more beneficial than film cooling, a direct comparison needs to be made. As mentioned earlier, the blowing ratio calculation was based on a film cooling sample and later, for the transpiration cooling, same parameters were used[2]. Three different blowing ratios will be compared M=0.5, M=1 and M=2.

In Figure 5.20a laterally averaged film cooling effectiveness for all the transpiration sample and a film cooling sample at a blowing ratio M=0.5 is shown. Interestingly, film cooling outperforms transpiration cooling, especially in the far downstream region beginning at $\frac{x}{L} = 10$. While keeping the laterally averaged heat transfer coefficient nearly the same as for the transpiration cooling, which is shown in Figure 5.20b.

For blowing ratio M=1, the performance of the film cooling sample degraded, almost halved. While performance of transpiration cooling samples improved as shown in Figure 5.21a. However, with an increase in film cooling effectiveness, for transpiration cooling samples there was also an increase in heat transfer coefficient, while the heat transfer coefficient for film cooling slightly decreased, as can be seen in Figure 5.21b.

When further increasing the blowing ratio to M=2, laterally averaged film cooling effectiveness further decreases for the film cooling sample. Transpiration cooling samples also experience a decrease in this parameter, as can be seen in Figure 5.22a. The laterally averaged heat transfer coefficient stayed nearly the same for the film cooling sample, whereas for transpiration cooling samples there was an increase, as shown in Figure 5.22b.

Only for blowing ratio M=0.5 film cooling effectiveness was higher for the film cooling sample than for the transpiration samples. However, transpiration cooling samples were performing better at the higher blowing ratios. For the film cooling sample, the laterally averaged heat transfer coefficient was not affected by the increase in the blowing ratio. However, for the transpiration cooling, the increase in the blowing ratio resulted in the increase of laterally averaged heat transfer coefficient.

[2] Same blowing ratio indicates same coolant mass flow rate for each sample in this comparison

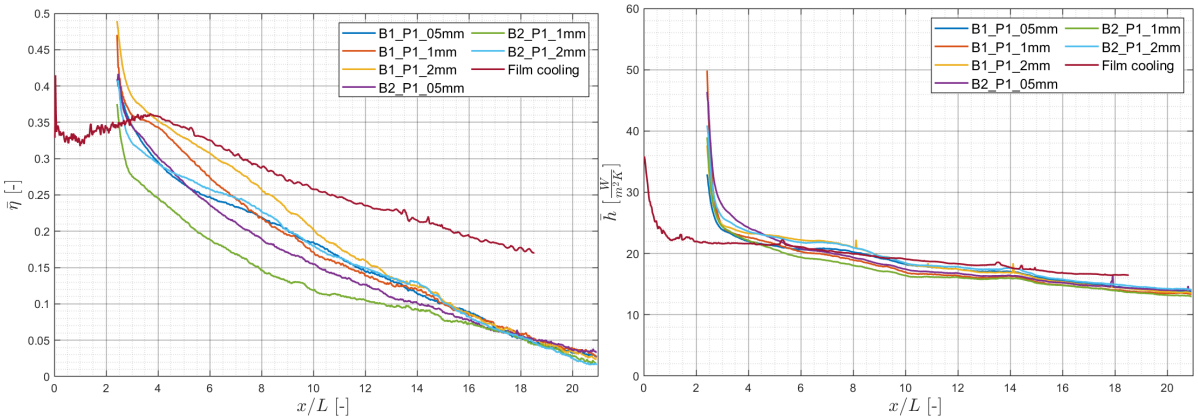

(a) *Film cooling effectiveness laterally averaged comparison with the film cooling blowing ratio M=0.5*

(b) *heat transfer coefficient laterally averaged comparison with the film cooling blowing ratio M=0.5*

Figure 5.20: *Film vs transpiration cooling for M=0.5*

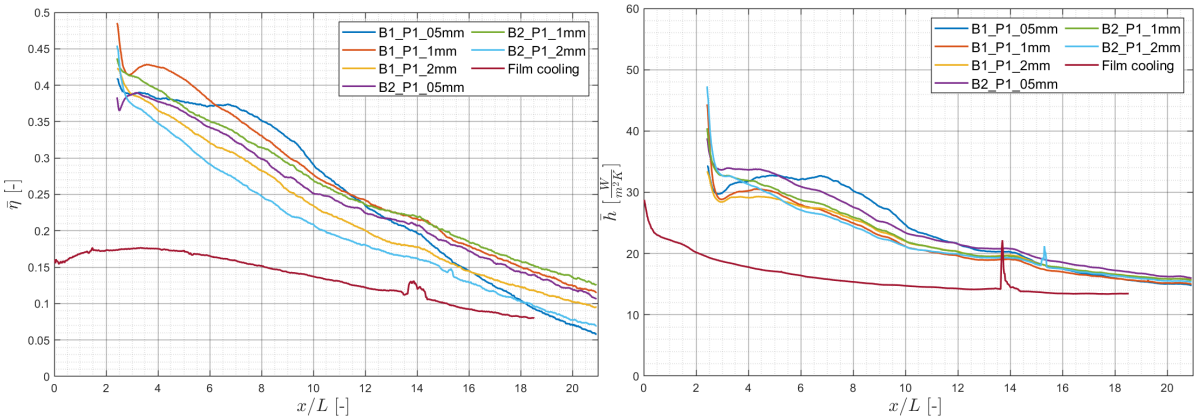

(a) *Film cooling effectiveness laterally averaged comparison with the film cooling blowing ratio M=1*

(b) *Heat transfer coefficient laterally averaged comparison with the film cooling blowing ratio M=1*

Figure 5.21: *Film vs transpiration cooling for M=1*

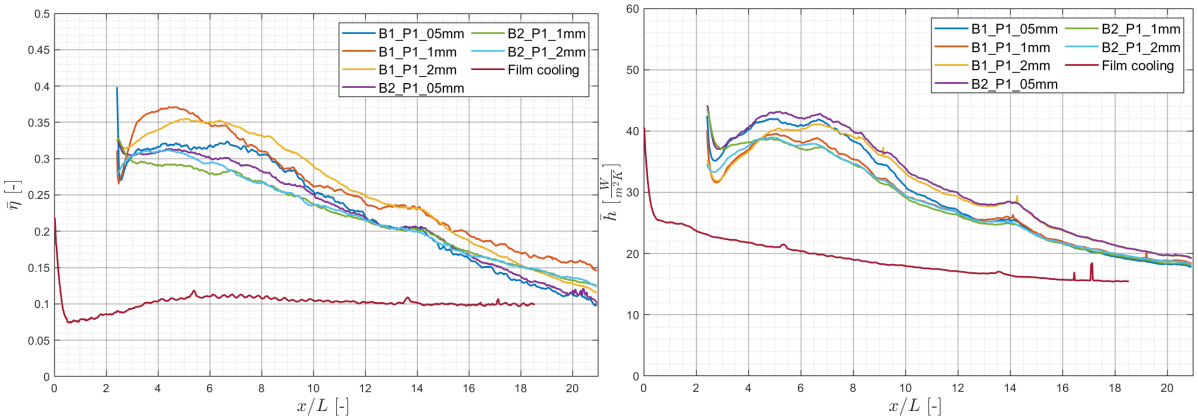

(a) *Film cooling effectiveness laterally averaged comparison with the film cooling blowing ratio M=2*

(b) *Heat transfer coefficient laterally averaged comparison with the film cooling blowing ratio M=2*

Figure 5.22: *Film vs transpiration cooling for M=2*

6

Discussion

For both batches the results for the laterally averaged film cooling effectiveness and laterally averaged heat transfer coefficient displayed the same trends, suggesting that the materials used were too similar in terms of their properties.

The results for laterally averaged film cooling effectiveness for lower blowing ratios have a linear trend as opposed to results for higher blowing ratios. There was an increase in the average results when increasing the blowing ratio from M=0.5 to M=1, which indicates that higher blowing ratios are beneficial for the performance. For higher blowing ratios the results show vastly different trends. The behaviour for laterally averaged film cooling effectiveness for higher blowing ratios can be associated with the coolant lifting of the surface of the TLC and reattaching further downstream. Similar behaviour can be observed in the film cooling case for high blowing ratios. When the coolant has high velocity, it lifts off the surface, resulting in lower film cooling effectiveness in the initial region, and then reattaches, improving the film cooling effectiveness. Additionally, in Figure 5.1b and 5.4b in the initial region, results for blowing ratio M=2, were higher than the results for the blowing ratio M=3.5. So a further increase in the blowing ratio lowered the initial performance. Therefore, together with the results for lower blowing ratios, this suggests that there is an optimal blowing ratio, somewhere between M=1 and M=2, that will result in the highest film cooling effectiveness.

For the laterally averaged heat transfer coefficient, increasing the blowing ratio increased the heat transfer coefficient. This behaviour can be associated with how the two flow loops mix together. With a higher blowing ratio, the coolant flow has a higher velocity, which will result in more violent mixing with the mainstream flow.

The laterally averaged heat flux ratio showed that only lower blowing ratios would be considered beneficial for the overall cooling performance. The high values of laterally averaged heat flux ratio for higher blowing ratios, M=2 and M=3.5 are associated with significantly higher heat transfer coefficient as compared to lower blowing ratios.

Different thicknesses of the porous structures had no influence on the global trends for the laterally averaged film cooling effectiveness or the laterally averaged heat transfer coefficient. However, with water visualisation results, it can be noticed that the lower thicknesses seem to have a more uniform pore distribution. Whereas for the samples with the highest thickness of $t_p = 2mm$ there are gaps forming between the water jets. Although these gaps had no influence on the averaged parameters, their effects were visible during experiment and, later, in the post-processed 2D colour maps. In Figure 6.1 a picture of the test section for sample B2_P1_2mm at blowing ratio M=1 is visible. The colourful peak in the middle of the sample is associated with the area without any through-pores pointed in the Figure 5.18. That peak is then visible in the post-processed 2D colour map of film cooling effectiveness (Figure 6.2 as the colour trough at about 160 pixel. This areas have local, but critical, influence on the results obtained. The inconsistency in the through-pores distribution is most likely linked to the manufacturing process. Since the build direction and printing parameters are confidential it is impossible to draw further conclusions.

Figure 6.1: *Picture of the test section sample B2_P1_2mm, blowing ratio M=1*

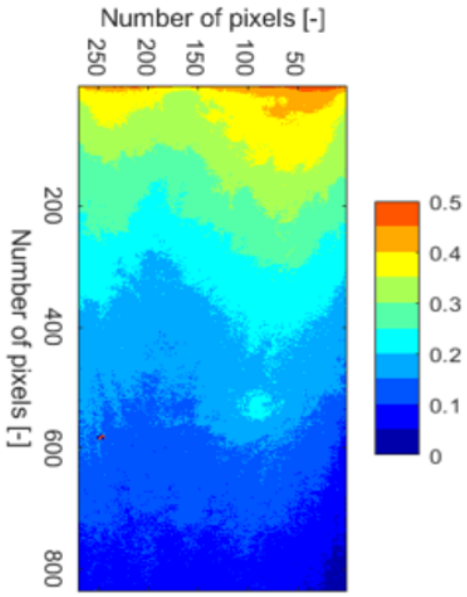

Figure 6.2: *Film cooling effectiveness, post-processed 2D colour map, sample B2_P1_2mm, blowing ratio M=1*

Last aspect of comparison for transpiration cooling is the flow through area. When the flow through area was decreased, the cooling performance decreased; the laterally averaged film cooling effectiveness decreased while the laterally averaged heat transfer coefficient increased. When looking at Figure 5.8, one can see that the results for the plate with a lower flow through area have peaks in the laterally averaged film cooling effectiveness in the region right next the sample, which can be associated with coolant lifting of the surface. Since the sample had a lower flow through area, the coolant going through the sample had a much higher velocity at the same mass flow rate as compared to the sample with a higher flow through area. This resulted in more violent mixing with the mainstream flow. Unfortunately, it is not possible to determine the velocity of the coolant going through the sample, therefore, no conclusion can be drawn whether the results from both samples are aligned in the order of increasing/decreasing coolant velocity. The impact of reduced flow through area on the laterally averaged heat transfer coefficient is smaller. Although all the results for the sample with a lower flow through area are higher than their counterparts in the first region, the results for the same blowing ratios tends to converge in the downstream region. This can indicate that the heat transfer coefficient in the initial region is heavily influenced by the mixing of the two flows and how intense it is. However, in the downstream region, it seems like the amount of coolant in the system is more important.

Film cooling, as opposed to transpiration cooling, had low and stable laterally averaged heat transfer coefficient for all the blowing ratios. This can be associated with the flow through area and the way coolant is injected into the test section. In the film cooling, the flow through area is known and it is assumed to be much bigger than the flow through area of the transpiration samples. Due to the nature of the film cooling, the coolant is injected under $\alpha = 30^o$ with respect to the mainstream flow. This allows introducing the coolant into the test section in a calm way. Whereas for transpiration cooling, the coolant streams are directed randomly, with some being perpendicular to the mainstream flow, which results in a violent mixing of the two flows.

The uncertainty analysis as described in Appendix D.1 was conducted on the transpiration cooling results. The method used was developed by Moffat [59] and it is a variation of a root mean square method. This method aims to calculate the uncertainty of unknown quantities in terms of the uncertainty of the measured parameters. The average uncertainty of the heat transfer coefficient across all the samples and all the blowing ratios was found to be $U_h = 4.95\%$ whereas the average uncertainty for film cooling effectiveness was found to be $U_\eta = 0.027$.

In addition to the uncertainty study, a repeatability study was done. The repeatability study was conducted on a sample B1_P1_05mm for blowing ratio M=1. For the repeatability study, cold and hot tests were repeated with the same initial parameters: initial temperature of the test plate, average coolant temperature and average mainstream temperature. Results for the laterally averaged heat transfer coefficient can be seen in figure 6.3a, whereas the results for laterally averaged film cooling effectiveness can be seen in figure 6.3b. The repeatability results fall within the laterally averaged uncertainty intervals for both parameters. The repeatability study confirms that the experimental rig gives consistent results for the same input parameters.

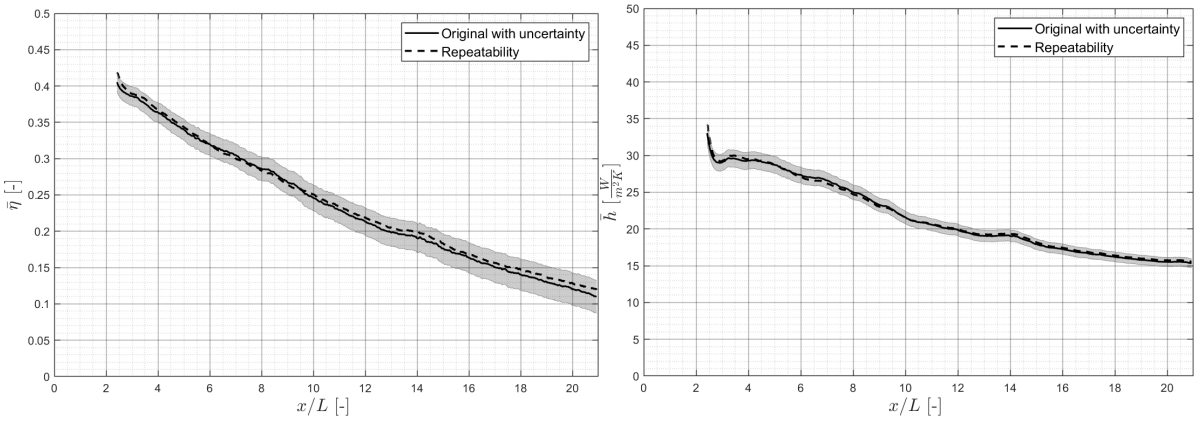

(a) *Repeatability results for laterally averaged film cooling effectiveness*

(b) *Repeatability results for laterally averaged heat transfer coefficient*

Figure 6.3: *Repeatability results*

Furthermore, a sensitivity study was also done on sample B2_P1_05mm. For this study, one parameter from one of the tests was changed at a time and new heat transfer coefficient and film cooling effectiveness were calculated. To save computational time, this was done only for three pixels. In this study, the inter-dependencies between parameters are neglected. The full description and the results of the sensitivity study can be found in Section D.3. This study showed that the outputs are the most influenced by the initial temperature of the test plate.

7

Conclusion and recommendations

The goal of this research was to investigate the cooling performance of additively manufactured porous structures. In order to achieve that, the heat transfer coefficient and film cooling effectiveness were determined and the heat flux ratio was calculated. The experiment was repeated using samples manufactured with two different materials, using different printing parameters and having different thicknesses of the porous structure. Each sample was tested at different blowing ratios to find an optimal operating conditions.

Blowing ratio had the biggest influence on the results. It was shown that increasing the blowing ratio, which meant increasing the coolant mass flow, increased the heat transfer coefficient. However, the influence of the blowing ratio on the film cooling effectiveness appeared to have a complicated nature. When the blowing ratio was increased from M=0.5 to M=1, the laterally averaged film cooling effectiveness increased, but when the blowing ratio was increased further to M=2 the effectiveness diminished as well as it changed the global trend, suggesting flow attachment issues. Similarly, when the blowing ratio increased to M=3.5, the laterally averaged film cooling effectiveness decreased even further.

After correcting the results from the hot test with the results from the heat loss test, the thickness of the porous structure seemed to have little to no effect on the global trends for the laterally averaged heat transfer coefficient or laterally averaged film cooling effectiveness. All the samples with the similar flow through areas but different thicknesses performed nearly the same at the same blowing ratio. However, thicker samples proved to have non-uniform distributions of the through pores, which can result in the uneven cooling performance.

Two different materials were used to manufacture the samples: Hastelloy-X and Inconel 625. Both of them were nickel-based alloys. They proved to give similar cooling performance in terms of the laterally averaged heat transfer coefficient and laterally averaged film cooling effectiveness at the same blowing ratio.

Flow through area is an important parameter when comparing cooling performance of the porous structures. A decrease in the flow through area had a negative impact on both of the parameters. Resulting in diminished laterally averaged heat transfer coefficient and laterally averaged film cooling effectiveness at all the blowing ratios as compared to a sample with a higher flow through area.

When comparing transpiration cooling against film cooling, the former outperformed the latter for blowing ratio M=1 and M=2 in laterally averaged film cooling effectiveness. However, transpiration cooling samples experienced a significant increase in laterally average heat transfer coefficient, when that parameter stayed nearly constant for all the blowing ratios for the film cooling sample.

Future work

For this research there are two major points of improvements and future developments. The first one is related to the flow through area of the samples. It is necessary to calculate or measure the flow through areas of the samples in order to compare the results to the film cooling sample. When knowing the flow through

area the coolant mass flow can be adjusted to accurately reproduce the same blowing ratio for transpiration cooling sample. Further studies into the sample should include:

1. Assessing how different thicknesses of the porous structure influence the flow through area
2. Mapping of the through pores in the samples
3. How the printing parameters, positions in the build chamber and quality of the powder influence the porosity and the distributions of the pores

The second future development is related to flow visualisation which can be done either experimentally or using Computational Fluid Dynamics (CFD) software. If the CFD software is used, the topology of the samples would need to be converted to the CAD model, which can be done using an advanced Computed Tomography. If the experimental method is to be explored, the optimal medium to visualise flows needs to be chosen (the medium cannot clog the pores etc.) together with the corresponding image acquisition equipment.

Bibliography

[1] R. S. Bunker, *Gas Turbine Engines: Turbine Cooling*. WIT Press, Dec. 2010, vol. 42, p. 199. DOI: 10.1002/9780470686652.eae093.

[2] B. L. Koff, "Gas turbine technology evolution: A designers perspective", *Journal of Propulsion and Power*, vol. 20, pp. 577–595, Jul. 2004. DOI: 10.2514/1.4361.

[3] B. Lakshminarayana, *Fluid Dynamics and Heat Transfer of Turbomachinery*. John Wiley & Sons, Inc., Dec. 1995. DOI: 10.1002/9780470172629.

[4] S. Baheri, S. P. A. Tabrizi, and B. A. Jubran, "Film cooling effectiveness from trenched shaped and compound holes", *Heat and Mass Transfer*, vol. 44, pp. 989–998, Sep. 2007. DOI: 10.1007/s00231-007-0341-9. [Online]. Available: https://www.researchgate.net/publication/200002136_Film_Cooling_Effectiveness_from_Trenched_Shaped_and_Compound_Holes (visited on 03/01/2021).

[5] J. Wang, K. Tian, J. Luo, and B. Sundén, "Effect of hole configurations on film cooling performance", *Numerical Heat Transfer, Part A: Applications*, vol. 75, pp. 725–738, Jun. 2019. DOI: 10.1080/10407782.2019.1608762. (visited on 03/01/2021).

[6] J. C. Snyder and K. A. Thole, "Performance of public film cooling geometries produced through additive manufacturing", *Journal of Turbomachinery*, vol. 142, Apr. 2020. DOI: 10.1115/1.4046488. (visited on 03/01/2021).

[7] R. Schroeder and K. Thole, "Adiabatic effectiveness measurements for a baseline shaped film cooling hole", *Proceedings of ASME Turbo Expo 2014: Turbine Technical Conference and Exposition, ASME, Düsseldorf, Germany, June 16, pp. 1–13.*, 2014.

[8] J. E. Sargison, S. M. Guo, M. L. G. Oldfield, G. D. Lock, and A. J. Rawlinson, "A converging slot-hole film-cooling geometry—part 2: Transonic nozzle guide vane heat transfer and loss", *Journal of Turbomachinery*, vol. 124, pp. 461–471, Jul. 2002. DOI: 10.1115/1.1459736. (visited on 03/23/2021).

[9] Y. Lu, H. Nasir, D. Faucheaux, and S. V. Ekkad, "Film cooling measurements for novel hole configurations", *Journal of Heat Transfer*, vol. 128, pp. 737–737, Aug. 2006. DOI: 10.1115/1.2221300. (visited on 03/23/2021).

[10] M. A. Hossain, R. Prenter, R. K. Lundgreen, A. Ameri, J. W. Gregory, and J. P. Bons, "Experimental and numerical investigation of sweeping jet film cooling", *Journal of Turbomachinery*, vol. 140, Dec. 2017. DOI: 10.1115/1.4038690. (visited on 03/23/2021).

[11] D. Thurman, P. Poinsatte, A. Ameri, D. Culley, S. Raghu, and V. Shyam, "Investigation of spiral and sweeping holes", *Journal of Turbomachinery*, vol. 138, Apr. 2016. DOI: 10.1115/1.4032839. (visited on 03/23/2021).

[12] J. D. Heidmann and S. Ekkad, "A novel antivortex turbine film-cooling hole concept", *Journal of Turbomachinery*, vol. 130, May 2008. DOI: 10.1115/1.2777194. (visited on 03/23/2021).

[13] L. Ding, K. Wei, Q. Zhang, and J. Wang, "An experimental investigation on transpiration cooling of porous flat plate", *2011 International Conference on Remote Sensing, Environment and Transportation Engineering*, Jun. 2011. DOI: 10.1109/rsete.2011.5965645. (visited on 03/01/2021).

[14] Z. Huang, Y.-h. Zhu, Y.-b. Xiong, and P.-X. Jiang, "Investigation of supersonic transpiration cooling through sintered metal porous flat plates", *Journal of Porous Media*, vol. 18, pp. 1047–1057, Jan. 2015. DOI: 10.1615/jpormedia.2015012159. (visited on 03/01/2021).

[15] G. Huang, Z. Min, L. Yang, P.-X. Jiang, and M. Chyu, "Transpiration cooling for additive manufactured porous plates with partition walls", *International Journal of Heat and Mass Transfer*, vol. 124, pp. 1076–1087, Sep. 2018. DOI: 10.1016/j.ijheatmasstransfer.2018.03.110. (visited on 03/01/2021).

[16] S. Haider, "K-electric, internship report", Main University Rd, NED University Of Engineering & Technology, Karachi, Karachi City, Sindh 75270, Pakistan, 2017.

[17] J. Hanania, K. Stenhouse, and J. Donev, *Gas turbine - energy education*, energyeducation.ca, Jul. 2018. [Online]. Available: https://energyeducation.ca/encyclopedia/Gas_turbine.

[18] A. Razak, *Industrial Gas Turbines*. Woodhead Publishing, 2007, pp. 120–136, ISBN: 9781845692056.

[19] M. Boyce, *Combined Cycle Systems for Near-Zero Emission Power Generation*. Woodhead Publishing, 2012, pp. 44–102, ISBN: 9780857090133.

[20] *Gas turbine handbook*, netl.doe.gov, May 2007. [Online]. Available: https://netl.doe.gov/coal/turbines/handbook (visited on 07/13/2021).

[21] L. Langston, *Each blade a single crystal*, American Scientist, Feb. 2017. [Online]. Available: https://www.americanscientist.org/article/each-blade-a-single-crystal (visited on 06/09/2021).

[22] H. J. Dai, N. D'Souza, and H. B. Dong, "Grain selection in spiral selectors during investment casting of single-crystal turbine blades: Part i. experimental investigation", *Metallurgical and Materials Transactions A*, vol. 42, pp. 3430–3438, Jun. 2011. DOI: 10.1007/s11661-011-0760-6. (visited on 07/13/2021).

[23] L. Hallcrest, *Handbook of Thermochromic Liquid Crystal Technology*. Hallcrest, 2014.

[24] *Rgb color model*, Wikipedia, Apr. 2021. [Online]. Available: https://en.wikipedia.org/wiki/RGB_color_model#/media/File:RGB_color_solid_cube.png.

[25] *Hsl and hsv*, Wikipedia, May 2021. [Online]. Available: https://en.wikipedia.org/wiki/HSL_and_HSV#/media/File:HSV_color_solid_cylinder_saturation_gray.png (visited on 05/20/2021).

[26] K. Li, "Experimental study of heat transfer coefficient and film cooling effectiveness", KTH School of Industrial Engineering and Management, 2019.

[27] G. Billot, "Experimental study on film cooling effectiveness and heat transfer coefficient distribution using thermochromic liquid crystals (tlc)", Politecnico di Milano, 2019.

[28] L. Gregurić, "Thow much does a metal 3d printer cost in 2020?", *https://all3dp.com/*, 2020. [Online]. Available: https://all3dp.com/2/how-much-does-a-metal-3d-printer-cost/.

[29] A. AB, *Arcam a2 setting the standard for additive manufacturing*. [Online]. Available: http://www.arcam.com/wp-content/uploads/Arcam-A2.pdf, accessed: 09.09.2020.

[30] M. Hall and D. Allinson, *Materials for Energy Efficiency and Thermal Comfort in Buildings*. Woodhead Publishing, 2010, ISBN: 9781845695262.

[31] T. Ghrib, *Porosity Process, Technologies and Applications*. IntechOpen, 2018, ISBN: 9781789230437.

[32] L. P. Lefebvre, J. Banhart, and D. Dunand, "Porous metals and metallic foams: Current status and recent developments", *Advanced Engineering Materials*, vol. 10, no. 9, pp. 775–787, 2008.

[33] D. A. Nealy and S. B. Reider, "Evaluation of laminated porous wall materials for combustor liner cooling", *Journal of Engineering for Power*, vol. 102, no. 2, pp. 268–276, 1980. [Online]. Available: https://www.hindawi.com/journals/ijp/2015/424628/.

[34] C. Poupinha, "Experimental study on film cooling and transpiration cooling through additively manufactured porous", Technical university of Lisbon, 2020.

[35] H. Carslaw and J. Jaeger, *Conduction of Heat in Solids*. Oxford, 1959, ISBN: 0198533683.

[36] Y. Yu, C. H. Yen, T. I. P. Shih, M. K. Chyu, and S. Gogineni, "Film cooling effectiveness and heat transfer coefficient distributions around diffusion shaped holes", *Journal Heat Transfer*, vol. 124, no. 5, pp. 820–82, 2002.

[37] G. Wagner, M. Kotulla, P. Ott, B. Weigand, and J. von Wolfersdorf, "The transient liquid crystal technique: Influence of surface curvature and finite wall thickness", *Journal of Turbomachinery*, vol. 127, no. 1, pp. 175–182, 2005.

[38] Y. Huang, S. Ekkad, and J.-C. Han, "Detailed heat transfer distributions under an array of orthogonal impinging jets", *Journal of themophysics and heat transfer*, vol. 12, no. 1, pp. 74–79, 1998.

[39] Matlab. (). Optimization toolbox, [Online]. Available: http://www.ece.northwestern.edu/local-apps/matlabhelp/toolbox/optim/fsolve.html. accessed: 22.09.2020.

[40] Applied and computational mathematics emphasis, *Lab 1. trust-region methods*. [Online]. Available: http://www.acme.byu.edu/wp-content/uploads/2014/09/Vol2Lab19TrustRegion.pdf, accessed: 22.09.2020.

[41] Z. Chen, "An ultrafast maximum power point setting scheme for photovoltaic arrays using model parameter identification", *International Journal of Photoenergy*, 2015. [Online]. Available: https://www.hindawi.com/journals/ijp/2015/424628/.

[42] L. H. R. T̃. Products, *Tlc coated plyester sheets*, 2009. [Online]. Available: https://www.lcrhallcrest.com/wp-content/uploads/2019/02/TLC-Sheets-Information-Sheet.pdf, accessed: 22.09.2020.

[43] H. International, *Principal features hastelloy ® x alloy strong and oxidation resistance*, 2019. [Online]. Available: http://haynesintl.com/docs/default-source/pdfs/new-alloy-brochures/high-temperature-alloys/brochures/x-brochure.pdf?sfvrsn=15b829d4_40.

[44] C. I. Ltd, *Inconel 625 | alloy 625 | inconel 625 alloy*, www.corrotherm.co.uk. [Online]. Available: https://www.corrotherm.co.uk/grades/inconel-625 (visited on 07/14/2021).

[45] R. J. Vedula and D. E. Metzger, "A method for the simultaneous determination of local effectiveness and heat transfer distributions in three-temperature convection situations", *NASA ADS*, Jun. 1991. [Online]. Available: https://ui.adsabs.harvard.edu/abs/1991gatu.confR....V/abstract (visited on 07/14/2021).

[46] R. Sumner, "Processing raw images in matlab", Department of Electrical Engineering, UC Santa Cruz, 2014.

[47] L. Wright, S. McClain, and M. Clemenson, "Effect of density ratio on flat plate film cooling with shaped holes using psp", *Journal of Turbomachinery*, vol. 133, no. 4, 2011.

[48] A. Dhungel, Y. Lu, W. Phillips, S. Ekkad, and J. Heidmann, "Film cooling from a row of holes supplemented with antivortex holes", *Journal of Turbomachinery*, vol. 131, no. 2, 2009.

[49] S. Baldauf, M. Scheurlen, A. Schulz, and S. Wittig, "Correlation of film-cooling effectiveness from thermographic measurements at enginelike conditions", *Journal of Turbomachinery*, vol. 124, no. 4, pp. 686–698, 2002.

[50] S. Baldauf, M. Scheurlen, and A. Schulz, "Heat flux reduction from film cooling and correlation of heat transfer coefficients from thermographic measurements at engine like conditions", *Proceedings of the ASME Turbo Expo 2002: Power for Land, Sea, and Air*, vol. 3, pp. 163–174, 2002.

[51] H. Nasir, S. Acharya, and S. Ekkad, "Film cooling from a single row of cylindrical angled holes with triangular tabs having different orientations", *Proceedings of the ASME Turbo Expo 2001: Power for Land, Sea, and Air.*, 2001.

[52] M. Gritsch, A. Schulz, and S. Wittig, "Heat transfer coefficient measurement of film cooling holes with expanded slots", *Proceedings of the ASME 1998 International Gas Turbine and Aeroengine Congress and Exhibition.*, 1998.

[53] R. Goldstein, P. Jin, and R. Olson, "Film cooling effectiveness and mass/heat transfer downstream of one row of discrete holes", *Proceedings of the ASME 1998 International Gas Turbine and Aeroengine Congress and Exhibition*, 1998.

[54] M. Gritsch, A. Schulz, and S. Wittig, "Film cooling with compound angle holes: Adiabatic effectiveness", *Journal of Turbomachinery*, vol. 188, no. 4, pp. 807–813, 1996.

[55] H. Ammari, N. Hay, and D. Lampard, "The effect of density ratio on the heat transfer coefficient from a film-cooled flat plate", *Journal of Turbomachiney*, vol. 112, no. 1, pp. 444–450, 1985.

[56] N. Hay, D. Lampard, and C. Saluja, "Effects of cooling films and the heat transfer coefficient on a flat plate with zero mainstream pressure gradient", *Journal of Engineering for Gas Turbines Power*, vol. 107, no. 1, pp. 105–110, 1985.

[57] D. Pedersen, E. Eckert, and R. Goldstein, "Film cooling with large density differences between the mainstream and secondary fluid measured by the heat-mass transfer analogy", *ASME. Journal of Heat Transfer.*, vol. 99, no. 4, pp. 620–627, 1977.

[58] L. Eriksen and R. Goldstein, "Heat transfer and film cooling following injection through inclined circular tubes", *Journal of Heat Transfer*, vol. 96, no. 2, pp. 239–245, 1974.

[59] R. J. Moffat, "Describing the uncertainties in experimental results", *Experimental Thermal and Fluid Science*, vol. 1, pp. 3–17, Jan. 1988. DOI: 10.1016/0894-1777(88)90043-x.

A

Equation derivation

In this appendix the full equation derivation will be given.

A.1. Governing equations

The governing equations are:

$$\frac{\partial^2 T}{\partial z^2} = \frac{1}{\alpha}\frac{\partial T}{\partial t} \tag{A.1}$$

$$\lim_{z\to\infty} T(z,t) = T_i \tag{A.2}$$

$$T(z,0) = T_i \tag{A.3}$$

$$-\lambda\frac{\partial T(0,t)}{\partial z} = h\left(T_w - T(0,t)\right) \tag{A.4}$$

Equations A.5 and A.6 are used to substitute for T and T_w in equations A.1-A.4.

$$T^* = \frac{T - T_i}{T_i} \tag{A.5}$$

$$T^*_{aw} = \frac{T_w - T_i}{T_i} \tag{A.6}$$

Once substituted:

$$\frac{\partial^2 T^*}{\partial z^2} = \frac{1}{\alpha}\frac{\partial T^*}{\partial t} \tag{A.7}$$

$$\lim_{z\to\infty} T^*(z,t) = 0 \tag{A.8}$$

$$T^*(z,0) = 0 \tag{A.9}$$

$$-\lambda\frac{\partial T^*(0,t)}{\partial z} = h\left(T^*_{aw} - T^*(0,t)\right) \tag{A.10}$$

Applying the Laplace transform... to equations A.7-A.10 gives:

$$\frac{\partial^2 \dot{T}^*}{\partial z^2} = \frac{1}{\alpha}\left(s\dot{T}^* - T^*(z,0)\right) \tag{A.11}$$

$$\lim_{z\to\infty} \dot{T}^*(z,s) = 0 \tag{A.12}$$

$$T^*(z,0) = 0 \tag{A.13}$$

$$-\lambda\frac{\partial \dot{T}^*(0,s)}{\partial z} = h\left(\frac{T^*_{aw}}{s} - \dot{T}^*(0,s)\right) \tag{A.14}$$

According to equation A.13, equation A.11, the calculation can be simplified as equation A.15

$$\frac{\partial^2 \dot{T}^*}{\partial z^2} = \frac{s}{\alpha}\dot{T}^* \tag{A.15}$$

Assuming standard solution of a form of equation A.16 and combining it with equation A.14.

$$\dot{T}^*(z,s) = Ae^{-z\sqrt{\frac{s}{\alpha}}} + Be^{z\sqrt{\frac{s}{\alpha}}} \tag{A.16}$$

If z is increasing $\dot{T}^*$ should approach zero according to equation A.12, therefore $B = 0$:

$$\dot{T}^*(z,s) = Ae^{-z\sqrt{\frac{s}{\alpha}}} \tag{A.17}$$

After substituting $\dot{T}^*$ into equation A.14, yields a Laplace domain solution:

$$A = \frac{h}{\lambda}\cdot\frac{T^*_{aw}}{s\left(\frac{h}{\lambda}+\sqrt{\frac{s}{\alpha}}\right)} \tag{A.18}$$

$$\dot{T}^*(z,s) = \frac{h}{\lambda}\cdot\frac{T^*_{aw}}{s\left(\frac{h}{\lambda}+\sqrt{\frac{s}{\alpha}}\right)}e^{-z\sqrt{\frac{s}{\alpha}}} \tag{A.19}$$

Using the inverse Laplace transform [35]:

$$F(s) = L\left[f(t)\right] = \int_0^{+\infty} e^{-st} f(t)\,dt \tag{A.20}$$

$$F(s) = \frac{e^{-ax}}{s(a+b)}\,a = \sqrt{\frac{s}{c}} \tag{A.21}$$

$$f(t) = \frac{1}{b}\operatorname{erfc}\left[\frac{x}{2\sqrt{ct}}\right] - \frac{1}{b}e^{(bx+ctb^2)}\cdot\operatorname{erfc}\left[\frac{x}{2\sqrt{ct}} + b\sqrt{ct}\right] \tag{A.22}$$

The expression for $\dot{T}^*$ could be inverted into time domain, and form a function of temperature difference ratio:

$$\frac{T_w - T_i}{T_R - T_i} = \operatorname{erfc}\left[\frac{z}{2\sqrt{t\alpha}}\right] - \exp\left[\frac{hz}{\lambda} + \frac{h^2 t\alpha}{\lambda^2}\right]\operatorname{erfc}\left[\frac{z}{2\sqrt{t\alpha}} + \frac{h\sqrt{t\alpha}}{\lambda}\right] \tag{A.23}$$

Since the experiment only focuses on the surface condition, the z-dimension is equal to zero ($z = 0$), giving final form of equation:

$$\frac{T_w - T_i}{T_R - T_i} = 1 - \exp\left[\frac{h^2 t\alpha}{\lambda^2}\right] \operatorname{erfc}\left[\frac{h\sqrt{t\alpha}}{\lambda}\right] \tag{A.24}$$

A.2. Blowing ratio

The blowing ratio is defined as:

$$M = \frac{\rho_C v_C}{\rho_M v_M} \tag{A.25}$$

Where v_C is defined as:

$$v_C = \frac{q_C}{A_C} \tag{A.26}$$

Where q_M is a volumetric flow. It is a mass flow divided by the density.

$$q_C = \frac{\dot{m}_C}{\rho_C} \tag{A.27}$$

Therefore:

$$\rho_C v_C = \rho_C \frac{\frac{\dot{m}_C}{\rho_C}}{A_C} = \frac{\dot{m}_C}{A_C} \tag{A.28}$$

Similarly, the main flow can be calculated resulted in:

$$M = \frac{\dot{m}_C A_M}{\dot{m}_M A_C} \tag{A.29}$$

A.3. Reynolds number

The Reynolds number for the main flow is defined as:

$$Re_M = \frac{v_M D_h}{\nu_M} = 25000 \tag{A.30}$$

where D_h is hydraulic diameter, v_M is the velocity of the main flow, and ν_M is kinematic viscosity of the main flow. The hydraulic diameter is purely geometrical and is defined as:

$$D_h = \frac{2WH}{W + H} \tag{A.31}$$

W and H are the width and height of the main flow rectangular cross-section, respectively.

The velocity of the main flow is:

$$v_M = \frac{q_M}{WH} \tag{A.32}$$

Where q_M is a volumetric flow. It is a mass flow divided by the density.

$$q_M = \frac{\dot{m}_M}{\rho_M} \tag{A.33}$$

The mass flow is assumed to be constant throughout the experiment and the density of the main flow is defined as follows:

$$\rho = \frac{P_M + P_a}{T_M} \tag{A.34}$$

P_M and P_a are pressures of the main flow and ambient pressure, respectively. T_M is the temperature of the main flow expressed in Kelvins. The kinematic viscosity from equation A.30 is defined as dynamic viscosity divided by density.

$$\nu_M = \frac{\mu_M}{\rho_M} \tag{A.35}$$

With dynamic viscosity being defined by Sutherland's viscosity law. It depends on the input temperature.

$$\mu_M = K \frac{T_M^{1.5}}{T_M + s} \tag{A.36}$$

Both K and s are constants. $K = 1.458 \cdot 10^{-6} \frac{kgsK^{1/2}}{m}$, $s = 110.4K$
Reynolds number derivation for the coolant flow follows the same process.

B

Technical drawing of a sample

This appendix will provide a technical drawing of the transpiration cooling sample. The sample consists of a porous strip surrounded by solid metal frame.

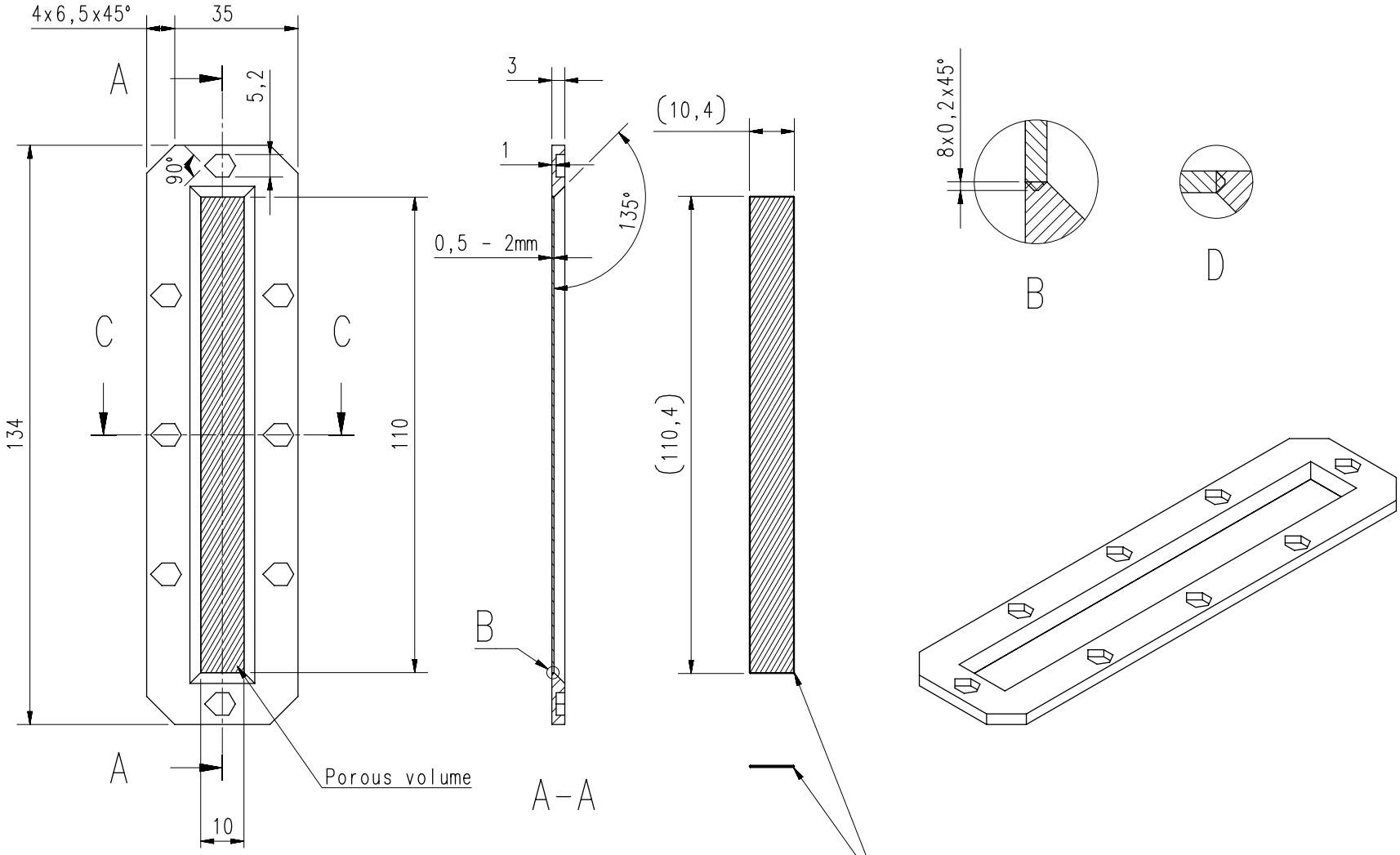

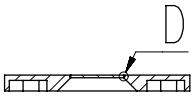

C-C

FSP	Date	Name	Scale 1:1	Based On			
Created			Title				
Reviewed			Test piece				Mass [kg]
Approved			Porous test piece				0.077
1st Appr							
	Size	Ident-Number/Document-Number			Revision	Language	Sheet
	A3	E1B100598463			A	en	1/1

C

Comparison plots Batch 1 vs. Batch 2

This appendix contains comparison plots for batch 1 vs batch 2 for samples with 0.5mm thickness and 2mm thickness. For all the samples, the values were calculated using batch 1 as a reference baseline, according to the Equation C.1.

$$\Delta\% = \frac{Batch2 - Batch1}{Batch1} \cdot 100\% \tag{C.1}$$

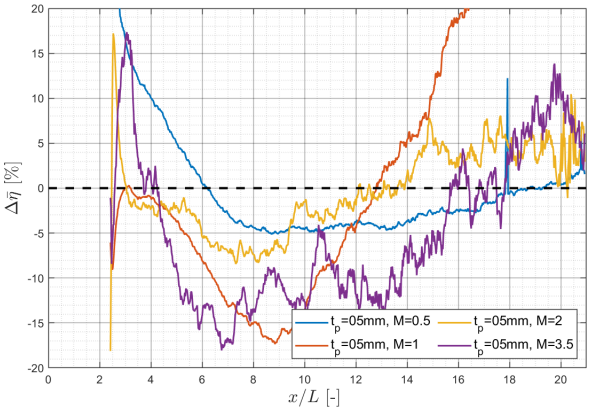

Figure C.1: *Batch 1 vs. Batch 2: Film cooling effectiveness laterally averaged - sample 0.5mm*

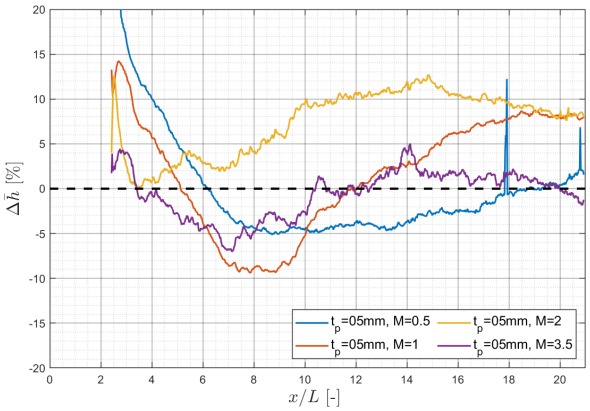

Figure C.2: *Batch 1 vs. Batch 2: Heat transfer coefficient laterally averaged - sample 0.5mm*

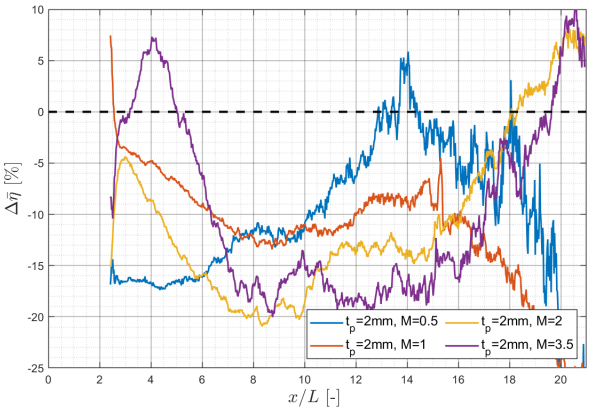

Figure C.3: *Batch 1 vs. Batch 2: Film cooling effectiveness laterally averaged - sample 2mm*

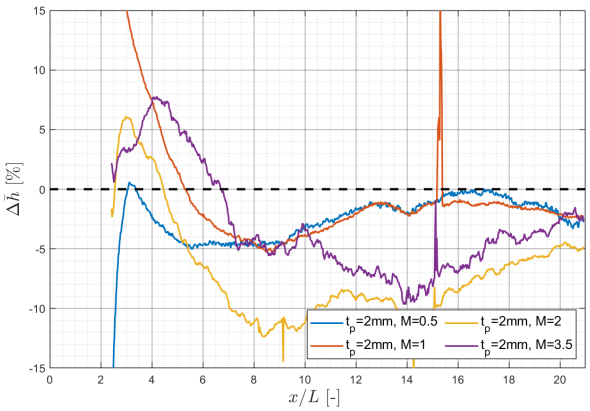

Figure C.4: *Batch 1 vs. Batch 2: Heat transfer coefficient laterally averaged - sample 2mm*

D

Uncertainty Analysis and sensitivity study

In this appendix uncertainty analysis is shown in Section D.1, followed by a sensitivity study shown in Section D.2.

D.1. Uncertainty analysis

The uncertainty analysis for the current study was performed according to the method developed by Moffat [59]. This method is using an implicit system of equations, represented by:

$$\begin{bmatrix} F_1(x_1, x_2, ..., x_m, p_1, p_2, ..., p_n) \\ \vdots \\ F_m(x_1, x_2, ..., x_m, p_1, p_2, ..., p_n) \end{bmatrix} = 0 \tag{D.1}$$

where F_m represents the implicit equations to determine the m-unknown physical quantities, x_m represents a set of calculated output parameters associated with the physical problem and and p_m represents a set of calculated input parameters. The system of equations for this problem was introduced in Section 3.1:

$$\begin{cases} F_1 = \left(1 - \exp\left[h^2 \frac{t_{g,c}}{\lambda \rho C_p}\right] \operatorname{erfc}\left[h\sqrt{\frac{t_{g,c}}{\lambda \rho C_p}}\right]\right) \cdot \left[\eta T_{C,c} + (1-\eta) T_{M,c} - T_{i,cold}\right] + T_{i,c} - T_w \\ F_2 = \left(1 - \exp\left[h^2 \frac{t_{g,h}}{\lambda \rho C_p}\right] \operatorname{erfc}\left[h\sqrt{\frac{t_{g,h}}{\lambda \rho C_p}}\right]\right) \cdot \left[\eta T_{C,h} + (1-\eta) T_{M,h} - T_{i,h}\right] + T_{i,h} - T_w \end{cases} \tag{D.2}$$

can be rewritten and represented by:

$$\begin{bmatrix} F_1\left(\eta, h, t_{g,c}, t_{g,h}, T_{C,c}, T_{C,h}, T_{M,c}, T_{M,h} T_{i,c}, T_{i,h}, T_w, \lambda, \rho, C_p\right) \\ F_2\left(\eta, h, t_{g,c}, t_{g,h}, T_{C,c}, T_{C,h}, T_{M,c}, T_{M,h} T_{i,c}, T_{i,h}, T_w, \lambda, \rho, C_p\right) \end{bmatrix} = 0 \tag{D.3}$$

with

$$x = [\eta, h] \tag{D.4}$$

$$p = \left[t_{g,c}, t_{g,h}, T_{C,c}, T_{C,h}, T_{M,c}, T_{M,h} T_{i,c}, T_{i,h}, T_w, \lambda, \rho, C_p\right] \tag{D.5}$$

Each of the measured parameters, p_i, has an associated experimental uncertainty U_{pi}. The goal is to determine the uncertainty associated with the unknowns η, h in terms of the uncertainties of the measured parameters and neglecting inter-dependencies between the parameters
First step in uncertainty analysis is implicit differentiation of equation D.3. This leads to a matrix equation of a form:

$$\begin{bmatrix} \frac{\delta F_1}{\delta x_1} & \cdots & \frac{\delta F_1}{\delta x_m} \\ \vdots & \ddots & \vdots \\ \frac{\delta F_m}{\delta x_1} & \cdots & \frac{\delta F_m}{\delta x_m} \end{bmatrix} \begin{bmatrix} dx_1 \\ \vdots \\ dx_m \end{bmatrix} + \begin{bmatrix} \frac{\delta F_1}{\delta p_1} & \cdots & \frac{\delta F_1}{\delta p_m} \\ \vdots & \ddots & \vdots \\ \frac{\delta F_m}{\delta p_1} & \cdots & \frac{\delta F_m}{\delta p_m} \end{bmatrix} \begin{bmatrix} dp_1 \\ \vdots \\ dp_m \end{bmatrix} = 0 \tag{D.6}$$

or in the simplified form:

$$\big[S\big]\,dX + [P]dP = 0 \tag{D.7}$$

Where $[S]$ is the output sensitivity matrix defined as

$$[S] = \begin{bmatrix} \frac{\delta F_1}{\delta x_1} & \cdots & \frac{\delta F_1}{\delta x_m} \\ \vdots & \ddots & \vdots \\ \frac{\delta F_m}{\delta x_1} & \cdots & \frac{\delta F_m}{\delta x_m} \end{bmatrix} = \begin{bmatrix} \frac{\delta F_1}{\delta \eta} & \frac{\delta F_1}{\delta h} \\ \frac{\delta F_2}{\delta \eta} & \frac{\delta F_2}{\delta h} \end{bmatrix} \tag{D.8}$$

and $[P]$ is the input sensitivity matrix defined as:

$$P = \begin{bmatrix} \frac{\delta F_1}{\delta p_1} & \cdots & \frac{\delta F_1}{\delta p_m} \\ \vdots & \ddots & \vdots \\ \frac{\delta F_m}{\delta p_1} & \cdots & \frac{\delta F_m}{\delta p_m} \end{bmatrix} = \begin{bmatrix} \frac{\delta F_1}{\delta t_{g,c}} & \cdots & \frac{\delta F_1}{\delta C_p} \\ \frac{\delta F_2}{\delta t_{g,c}} & \cdots & \frac{\delta F_2}{\delta C_p} \end{bmatrix} \tag{D.9}$$

and $dX = [dx_1 \dots dx_m]^t$ and $dP = [dp_1 \dots dp_m]^t$ are the deviation vectors associated with the differential changes in the dependent variables and the independent parameters respectively. Reordering equation D.7 and solving for the dependent variable yields to:

$$dX = -[S]^{-1}[P]dP = [K]dP \tag{D.10}$$

where $[K]$ is the overall sensitivity matrix relating deviations i the independent parameter variables ($t_{g,c}$,..., C_p) to the deviations in the dependent variables (η and h). The derivatives calculations are presented in appendix E.

The next step, is to calculate the room-mean square uncertainty. It is assumed that the differential changes represented by the deviation vectors are small and independent. The differential changes are assumed to represent the solution errors due to errors in the independent parameters, which are expressed as:

$$\begin{bmatrix} \eta - \hat{\eta} \\ h - \hat{h} \end{bmatrix} = \begin{bmatrix} K_{1,1} & \dots & K_{1,12} \\ \vdots & \ddots & \vdots \\ K_{2,1} & \dots & K_{2,12} \end{bmatrix} \begin{bmatrix} t_{g,c} - \hat{t_{g,c}} \\ \vdots \\ C_p - \hat{C_p} \end{bmatrix} \tag{D.11}$$

where $\hat{x_i}$ ($\hat{\eta}$, $\hat{h}$) and $\hat{p_i}$ represent the true value of the solution variables and the independent variables respectively. The mean square deviations, σ^2, is written as:

$$\begin{bmatrix} \overline{\eta - \hat{\eta}} \\ \overline{h - \hat{h}} \end{bmatrix} = \begin{bmatrix} \sigma_\eta^2 \\ \sigma_h^2 \end{bmatrix} = \begin{bmatrix} K_{1,1}^2 & \dots & K_{1,12}^2 \\ \vdots & \ddots & \vdots \\ K_{2,1}^2 & \dots & K_{2,12}^2 \end{bmatrix} \begin{bmatrix} \overline{t_{g,c} - \hat{t}_{g,c}} \\ \vdots \\ \overline{C_p - \hat{C_p}} \end{bmatrix} = [K^2] \begin{bmatrix} \sigma_{t_{g,c}}^2 \\ \vdots \\ \sigma_{C_p}^2 \end{bmatrix} = [K^2]\delta P_i \tag{D.12}$$

where $[K^2]$ is the matrix of the squared sensitivity coefficients. Multiplication of the standard deviation associated with each variable by an appropriate t-value yields an estimate of the bound, or absolute uncertainty, at an appropriate level of confidence. Equation D.12 then becomes:

$$\begin{bmatrix} U_\eta^2 \\ U_h^2 \end{bmatrix} = [U_x^2] = \begin{bmatrix} K_{1,1}^2 & \dots & K_{1,12}^2 \\ \vdots & \ddots & \vdots \\ K_{2,1}^2 & \dots & K_{2,12}^2 \end{bmatrix} \begin{bmatrix} U_{t_{g,c}}^2 \\ \vdots \\ U_{C_p}^2 \end{bmatrix} = [K^2][U_p^2] \tag{D.13}$$

where U_{x_i} and U_{p_j} are the absolute uncertainties of the equation system solution and the independent measured parameters, respectively.

When performing a measurement, two components of uncertainty must be considered. Fist one is a systematic offset, which is provided by the manufacturers specification. It is commonly refereed to type B uncertainty, and it is summarised in the table D.1. The second uncertainty is a random error, so called uncertainty type A, summarised in table D.2 and it is related to the boundary conditions of the experiment. Following, Moffat's interpretation, the error descriptors were reported with a confidence level of 95%, meaning that the random uncertainty is expressed as 2σ, where σ is the standard deviation. The following corrected sample

standard deviation of a set of repeated N number of trials is taken to be representative of the random uncertainty of the quantity X_i

$$U_{Pi} = \sqrt{(U_{Pi,fixed})^2 + 2\sigma_i^2} \tag{D.14}$$

Table D.1: *Uncertainties type B – Fixed Uncertainties*

	Type B-$U_{pi,fixed}$
PT-100	$\pm 0.05^oC$
Thermocouple K	$\pm 0.2^oC$

Table D.2: *Uncertainties type A – Random Uncertainties*

Parameter	Type A-σ_i
$t_{g,c}$	±2.5%
$t_{g,h}$	±2.5%
$T_{C,c}$	±0.1
$T_{C,h}$	±0.1
$T_{M,c}$	±0.1
$T_{M,h}$	±0.1
$T_{i,c}$	±0.1
$T_{i,h}$	±0.1
T_w	±0.05
λ	±5%
ρ	±3%
C_p	±3%

That gives:

$$[U_x] = \begin{bmatrix} U_\eta \\ U_h \end{bmatrix} = \begin{bmatrix} \sqrt{K_{1,1}^2 U_{t_{g,c}}^2 + \ldots K_{1,12}^2 U_{C_p}^2} \\ \sqrt{K_{2,1}^2 U_{t_{g,c}}^2 + \ldots K_{2,12}^2 U_{C_p}^2} \end{bmatrix} \tag{D.15}$$

The average uncertainty of for the heat transfer coefficient across all the samples and all the blowing ratios was found to be U_h = 4.95% whereas the average uncertainty for film cooling effectiveness was found to be U_η = 0.027.

D.2. Sensitivity study

A sensitivity study was conducted on sample B2_P1_05mm. For the sensitivity study the original output parameters: heat transfer coefficient and film cooling effectiveness, were taken as a baseline. During the sensitivity study, one parameter from one of the tests (either from a cold or from a hot test) was changed and new heat transfer coefficient and film cooling effectiveness were calculated. The results of sensitivity study are shown as a percentage change with respect to the baseline values. In table D.3, results for 3 pixels located along same stream-wise line and averaged results for all of the pixels are present.

Table D.3: *Results sensitivity study*

		Pixel (135,45)		**Pixel (135,395)**		Pixel (135,795)		Averaged (all points)	
		%Htc	%Eta	%Htc	%Eta	%Htc	%Eta	%Htc	%Eta
Cold test	$T_{m,c}-0.256$	-0.14	-1	-0.1	-1.78	-0.06	-2.89	-0.11	-2.1
	$T_{m,c}+0.25$	0.14	0.99	0.1	1.76	0.06	2.85	0.1	2.07
	$T_{c,c}-0.25$	-0.09	-0.64	-0.03	-0.62	-0.01	-0.59	-0.04	-0.62
	$T_{c,c}+0.25$	0.09	0.64	0.04	0.63	0.01	0.6	0.04	0.63
	$T_{i,c}-0.25$	-0.31	-2.18	-0.25	-4.42	-0.16	-7.61	-0.26	-5.34
	$T_{i,c}+0.25$	0.31	2.16	0.25	4.4	0.16	7.58	0.26	5.31
	$t_{g,c}-1$	-0.08	-0.55	-0.05	-0.81	-0.02	-1.15	-0.05	-1.05
	$t_{g,c}-0.1$	-0.01	-0.05	0	-0.08	0	-0.11	-0.01	-0.1
	$t_{g,c}+0.1$	0.01	0.05	0	0.08	0	0.11	0.01	0.1
	$t_{g,c}+1$	0.08	0.54	0.05	0.8	0.02	1.14	0.05	1.03
Hot test	$T_{m,h}-0.25$	0.59	0.55	0.64	1.24	0.66	2.29	0.65	1.56
	$T_{m,h}+0.25$	-0.59	-0.56	-0.64	-1.25	-0.66	-2.31	-0.64	-1.58
	$T_{c,h}-0.25$	0.38	0.36	0.23	0.44	0.14	0.48	0.23	0.44
	$T_{c,h}+0.25$	-0.38	-0.36	-0.22	-0.44	-0.14	-0.48	-0.23	-0.44
	$T_{i,h}-0.25$	2.49	2.3	2.44	4.65	2.35	7.98	2.45	5.6
	$T_{i,h}+0.25$	-2.5	-2.43	-2.45	-4.9	-2.36	-8.39	-2.45	-5.9
	$t_{g,h}-1$	2.39	2.21	1.05	2.03	0.63	2.18	1.29	2.39
	$t_{g,h}-0.1$	0.26	0.24	0.1	0.2	0.07	0.23	0.13	0.24
	$t_{g,h}+0.1$	-0.24	-0.22	-0.1	-0.2	-0.06	-0.22	-0.13	-0.24
	$t_{g,c}+1$	-2.27	-2.2	-1.01	-1.99	-0.61	-2.15	-1.23	-2.37

This type of sensitivity study ignores inter-dependencies between parameters (for example when changing the coolant temperature (T_c), the time to reach maximum green intensity (t_g) will change as well). This sensitivity study shows that the initial temperature of the bottom plate (plate with the TLC sheet) is the most influential factor for both hot and cold test.

E

Derivatives

This appendix provides the derivatives used in the uncertainty analysis.

- $$\frac{\delta F}{\delta \eta} = (T_C - T_M)\left(1 - e^{\frac{t_g h^2}{\lambda \rho C_p}} erfc\left(h\sqrt{\frac{t_g}{\lambda \rho C_p}}\right)\right) \tag{E.1}$$
- $$\frac{\delta F}{\delta h} = (\eta T_C - T_M(1-\eta) - T_i))\left(2\sqrt{\frac{t_g}{\pi \lambda \rho C_p}} - \frac{2 t_g h}{\lambda \rho C_p} e^{\frac{t_g h^2}{\lambda \rho C_p}} erfc\left(h\sqrt{\frac{t_g}{\lambda \rho C_p}}\right)\right) \tag{E.2}$$
- $$\frac{\delta F}{\delta T_C} = \eta\left(1 - e^{\frac{t_g h^2}{\lambda \rho C_p}} erfc\left(h\sqrt{\frac{t_g}{\lambda \rho C_p}}\right)\right) \tag{E.3}$$
- $$\frac{\delta F}{\delta T_i} = e^{\frac{t_g h^2}{\lambda \rho C_p}} erfc\left(h\sqrt{\frac{t_g}{\lambda \rho C_p}}\right) \tag{E.4}$$
- $$\frac{\delta F}{\delta T_M} = (\eta - 1)\left(e^{\frac{t_g h^2}{\lambda \rho C_p}} erfc\left(h\sqrt{\frac{t_g}{\lambda \rho C_p}}\right) - 1\right) \tag{E.5}$$
- $$\frac{\delta F}{\delta \rho} = (\eta T_C - T_M(1-\eta) - T_i)\left(\frac{t_g h^2}{\lambda \rho^2 C_p} e^{\frac{t_g h^2}{\lambda \rho C_p}} erfc\left(h\sqrt{\frac{t_g}{\lambda \rho C_p}}\right) - \frac{t_g h}{\lambda \rho^2 C_p \sqrt{\frac{\pi t_g}{\lambda \rho C_p}}}\right) \tag{E.6}$$
- $$\frac{\delta F}{\delta C_p} = (\eta T_C - T_M(1-\eta) - T_i)\left(\frac{t_g h^2}{\lambda \rho C_p^2} e^{\frac{t_g h^2}{\lambda \rho C_p}} erfc\left(h\sqrt{\frac{t_g}{\lambda \rho C_p}}\right) - \frac{t_g h}{\lambda \rho C_p^2 \sqrt{\frac{\pi t_g}{\lambda \rho C_p}}}\right) \tag{E.7}$$
- $$\frac{\delta F}{\delta \lambda} = (\eta T_C - T_M(1-\eta) - T_i)\left(\frac{t_g h^2}{\lambda^2 \rho C_p} e^{\frac{t_g h^2}{\lambda \rho C_p}} erfc\left(h\sqrt{\frac{t_g}{\lambda \rho C_p}}\right) - \frac{t_g h}{\lambda^2 \rho C_p \sqrt{\frac{\pi t_g}{\lambda \rho C_p}}}\right) \tag{E.8}$$
- $$\frac{\delta F}{\delta t_g} = (\eta T_C - T_M(1-\eta) - T_i)\left(\frac{h}{\lambda \rho C_p \sqrt{\frac{\pi t_g}{\lambda \rho C_p}}} - \frac{h^2}{\lambda \rho C_p} e^{\frac{t_g h^2}{\lambda \rho C_p}} erfc\left(h\sqrt{\frac{t_g}{\lambda \rho C_p}}\right)\right) \tag{E.9}$$
- $$\frac{\delta F}{\delta T_w} = -1 \tag{E.10}$$